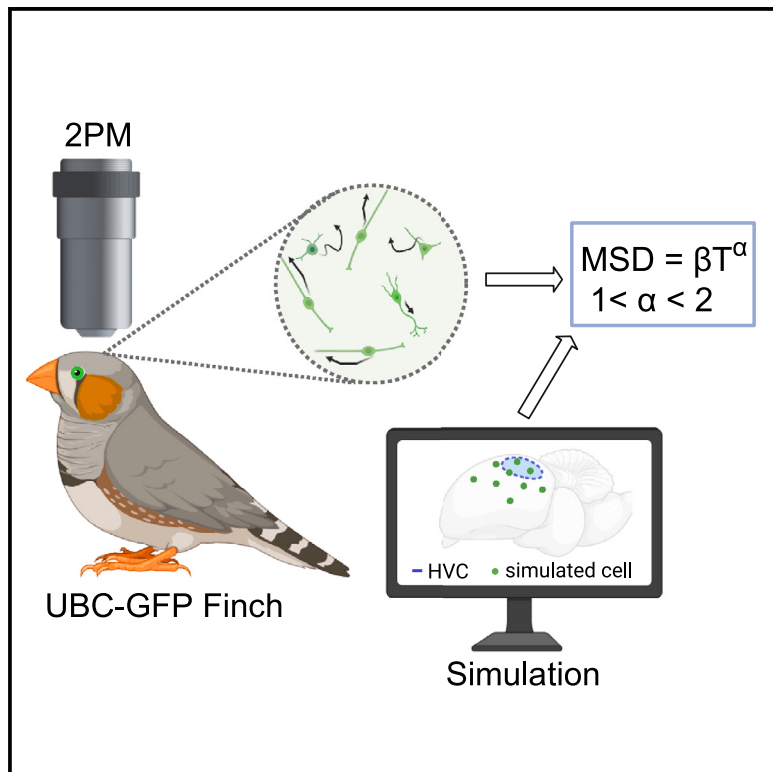


## In vivo imaging in transgenic songbirds reveals superdiffusive neuron migration in the adult brain

### Graphical abstract



### Authors

Naomi R. Shvedov, Sina Analoui,  
Theresia Dafalias, Brooke L. Bedell,  
Timothy J. Gardner, Benjamin B. Scott

### Correspondence

bbs@bu.edu

### In brief

Shvedov et al. employ two-photon microscopy to image the migration of hundreds of immature neurons in the brains of transgenic zebra finches. In the adult brain, this migration is widespread, with cells dispersing in all directions, and can be described mathematically as a superdiffusive process.

### Highlights

- Transgenic songbirds express GFP in a neurogenic lineage
- GFP expression is strong and sparse enough to track single cells *in vivo*
- Adult neuron migration is well fit by a superdiffusive model
- Superdiffusive migration is sufficient to populate song nucleus HVC in simulation



## Article

# In vivo imaging in transgenic songbirds reveals superdiffusive neuron migration in the adult brain

Naomi R. Shvedov,<sup>1</sup> Sina Analoui,<sup>2</sup> Theresia Dafalias,<sup>1</sup> Brooke L. Bedell,<sup>2</sup> Timothy J. Gardner,<sup>3</sup> and Benjamin B. Scott<sup>2,4,5,\*</sup>

<sup>1</sup>Graduate Program for Neuroscience, Boston University, Boston, MA 02215, USA

<sup>2</sup>Department of Psychological and Brain Sciences, Boston University, Boston, MA 02215, USA

<sup>3</sup>Phil and Penny Knight Campus for Accelerating Scientific Impact, University of Oregon, Eugene, OR 97403, USA

<sup>4</sup>Neurophotonics Center, Photonics Center, and Center for Systems Neuroscience, Boston University, Boston, MA 02215, USA

<sup>5</sup>Lead contact

\*Correspondence: bbs@bu.edu

<https://doi.org/10.1016/j.celrep.2024.113759>

## SUMMARY

Neuron migration is a key phase of neurogenesis, critical for the assembly and function of neuronal circuits. In songbirds, this process continues throughout life, but how these newborn neurons disperse through the adult brain is unclear. We address this question using *in vivo* two-photon imaging in transgenic zebra finches that express GFP in young neurons and other cell types. In juvenile and adult birds, migratory cells are present at a high density, travel in all directions, and make frequent course changes. Notably, these dynamic migration patterns are well fit by a superdiffusive model. Simulations reveal that these superdiffusive dynamics are sufficient to disperse new neurons throughout the song nucleus HVC. These results suggest that superdiffusive migration may underlie the formation and maintenance of nuclear brain structures in the postnatal brain and indicate that transgenic songbirds are a useful resource for future studies into the mechanisms of adult neurogenesis.

## INTRODUCTION

In the songbird, new neurons are continually added to forebrain circuits throughout life. These new neurons are added to a variety of regions, including HVC, a nucleus in the song circuit, which is involved in learned vocal communication.<sup>1</sup> In HVC, the addition of new projection neurons and interneurons is thought to play an important role in behavioral plasticity and tissue resilience.<sup>2–6</sup> These new neurons are born from neural stem cells in the ventricular zone (VZ) and migrate hundreds of micrometers to reach their integration targets in HVC and beyond.<sup>4,7</sup> How these new neurons migrate through the adult brain is unknown. Although neuron migration has been well studied in the vertebrate forebrain during development, the adult brain presents a different set of challenges to migration and integration and may involve new mechanisms.<sup>8</sup>

Previous histological and *in vitro* experiments in adult songbirds have described the close association of some young neurons with “radial glia” guide cells, similar to migration in the developing mammalian cortex.<sup>1,7,9</sup> However, many areas of the songbird brain that receive new neurons, including the song nucleus HVC, contain relatively few radial fibers, suggesting the possibility of other migratory mechanisms.<sup>10</sup> Retroviral labeling studies have revealed that migratory neurons in juvenile zebra finches follow tortuous paths that resemble a random walk and do not appear to exclusively follow radial fibers or blood vessels.<sup>11</sup> Together, these observations suggest the existence of a non-radial form of migration in the postnatal songbird

brain. However, a detailed description of this process and whether it continues into adulthood is lacking.

To address this question, we sought to quantitatively characterize the cellular dynamics of newborn neurons as they migrated through the brains of juvenile and adult zebra finches. We took advantage of a line of transgenic zebra finches that express green fluorescent protein (GFP) under the ubiquitin C (UBC) promoter.<sup>12</sup> The UBC-GFP transgenic strain was produced to demonstrate the efficiency of lentivirus-based transgenesis in songbirds, but GFP expression was not characterized in detail. Here we show that GFP is strongly expressed in a lineage that includes both young and mature neurons and that its expression is sparse enough and bright enough to enable single-cell tracking *in vivo*. We used time-lapse two-photon (2P) microscopy to follow populations of GFP-positive (GFP+) cells for up to 12 h as they migrated through the brain and applied a 3D manual tracking pipeline to quantify the migratory dynamics of over 800 migratory cells.

We found that migratory cells were present in high density within the juvenile and adult songbird brain. Migratory cells were not confined to a particular region or pathway but were found throughout the hyperpallium above HVC and the nidopallium in and around HVC, including in the brains of female birds. New neurons moved in different directions and made frequent turns, and their trajectories were well fit by a superdiffusive model. Finally, using statistics measured from *in vivo* data, we developed a quantitative simulation of the migration. This simulation revealed that this diffusive process was sufficient to



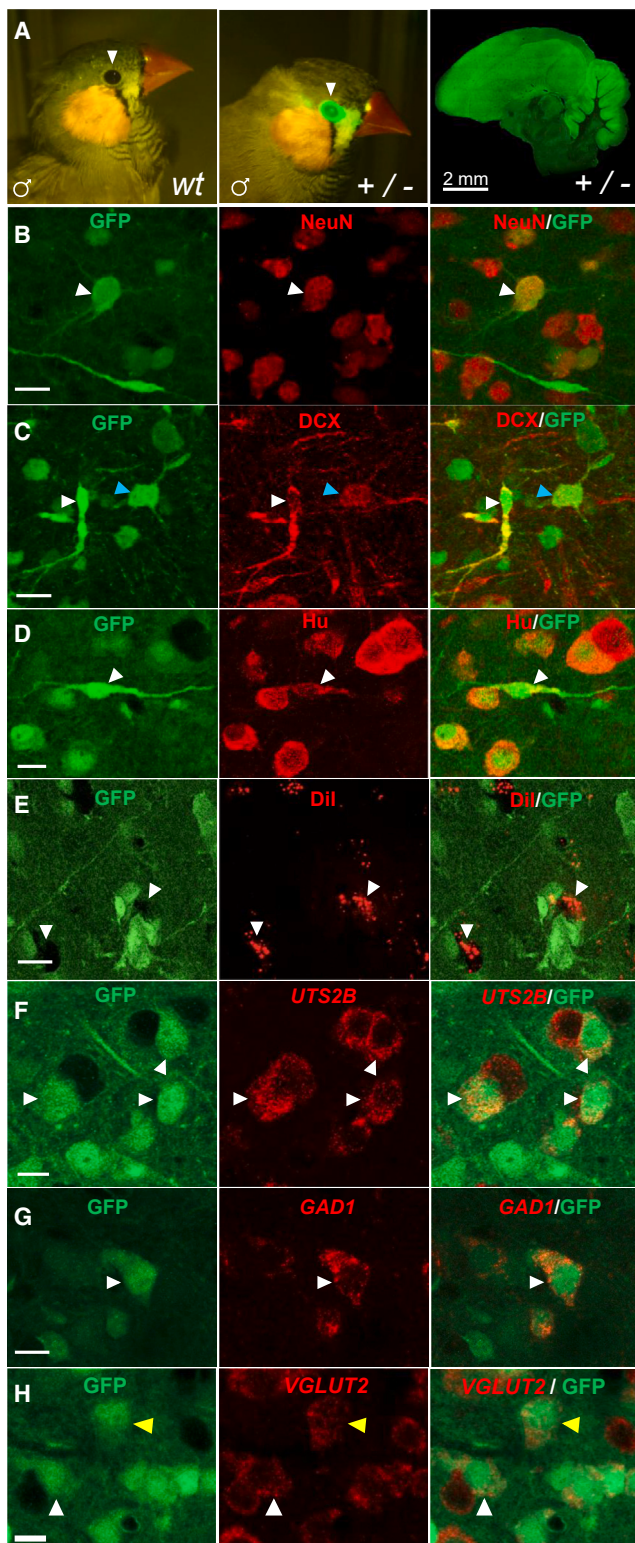


**Figure 1. UBC-GFP transgenic songbirds express GFP in a neurogenic lineage**

(A) Left: adult male wild-type finch under blue light excitation. No GFP fluorescence is observed (white arrowheads). Center: adult male transgenic finch under blue light excitation. Bright GFP fluorescence is observed around the

populate HVC within 3 weeks, the biologically relevant timescale for migration in songbirds.<sup>7</sup> Together, these results demonstrate a dynamic form of neuron migration that may allow flexible and efficient dispersal through the postnatal brain.

## RESULTS

### UBC-GFP transgenic songbirds express GFP in a neurogenic lineage

We first characterized GFP expression in the brains of UBC-GFP zebra finches in histological sections. We found that GFP was expressed throughout the forebrain, including the song nuclei, but varied across regions and cell types (Figures 1 and S1). In HVC, we quantified the percentage of different cell types that expressed GFP. Most GFP+ cells (90.8%, 188/207 cells, n = 1 bird) expressed Hu, a neuronal lineage marker that labels new neurons as well as mature neurons<sup>13</sup> (Figure 1D). A majority of GFP+ cells (64.2%, 258/402 cells, n = 4 birds) expressed NeuN, a marker for mature, post-migratory neurons<sup>14</sup> (Figure 1B). Half of GFP+ cells expressed VGLUT2, a marker for excitatory neurons (52%, n = 322/617 cells) (Figure 1H), and 23% of GFP+ cells expressed GAD1, a marker for inhibitory neurons (n = 143/617 cells) (Figure 1G).

Next, we evaluated GFP expression in three well-studied neuronal subtypes: HVC-to-RA glutamatergic projection neurons (HVC<sub>RA</sub>), HVC-to-area X glutamatergic projection neurons (HVC<sub>X</sub>), and GABAergic interneurons (HVC<sub>INT</sub>). No GFP+ cells were HVC<sub>X</sub> projection neurons that were retrogradely labeled from area X with Dil (n = 0/129 cells) (Figure 1E). We found that a subset of GFP+ cells were HVC<sub>RA</sub> projection neurons (27.1%, n = 196/724 cells), identified using FISH for Urotensin 2B (UTS2B) (Figure 1F). Another subset of GFP+ cells were likely HVC<sub>INT</sub>, identified using FISH for glutamate decarboxylase (GAD1) (23.2%, n = 143/617 cells) (Figure 1G).

In addition to mature neuron types, we also found that many GFP+ cells also expressed doublecortin (DCX) and were putative migratory neurons (41% of GFP+ cells expressed DCX; 174/424 cells, n = 4 birds). Although the density of labeling made complete morphological characterization difficult to achieve for all

eye (white arrowheads). Right: GFP expression found throughout the transgenic male adult brain.

(B) Mature neuron co-labeled with GFP and NeuN (white arrowheads). Scale bar, 10 μm.

(C) A GFP+ cell with bipolar neuron morphology labeled with DCX (white arrowheads) and a cell with multipolar morphology labeled with GFP and DCX (blue arrowheads). Scale bar, 10 μm.

(D) GFP+ bipolar cell co-labeled with Hu (white arrowheads). Scale bar, 10 μm.

(E) GFP-negative, Dil-labeled HVC<sub>X</sub> projectors (white arrowheads). Scale bar, 10 μm.

(F) Fluorescence *in situ* hybridization chain reaction (HCR-FISH) for UTS2B (red) and immunohistochemistry (IHC) staining for GFP (green). GFP+/UTS2B+ (HVC<sub>RA</sub> neurons) are indicated by white arrowheads. Scale bar, 10 μm.

(G) HCR-FISH for GAD1 (red) and IHC staining for GFP (green). GFP+/GAD1+ (mature interneurons) are indicated by white arrowheads. Scale bar, 10 μm.

(H) HCR-FISH for VGLUT2 (red) and IHC staining for GFP (green). GFP+/VGLUT2+ (mature excitatory neurons) are indicated by arrowheads. Scale bar, 10 μm.

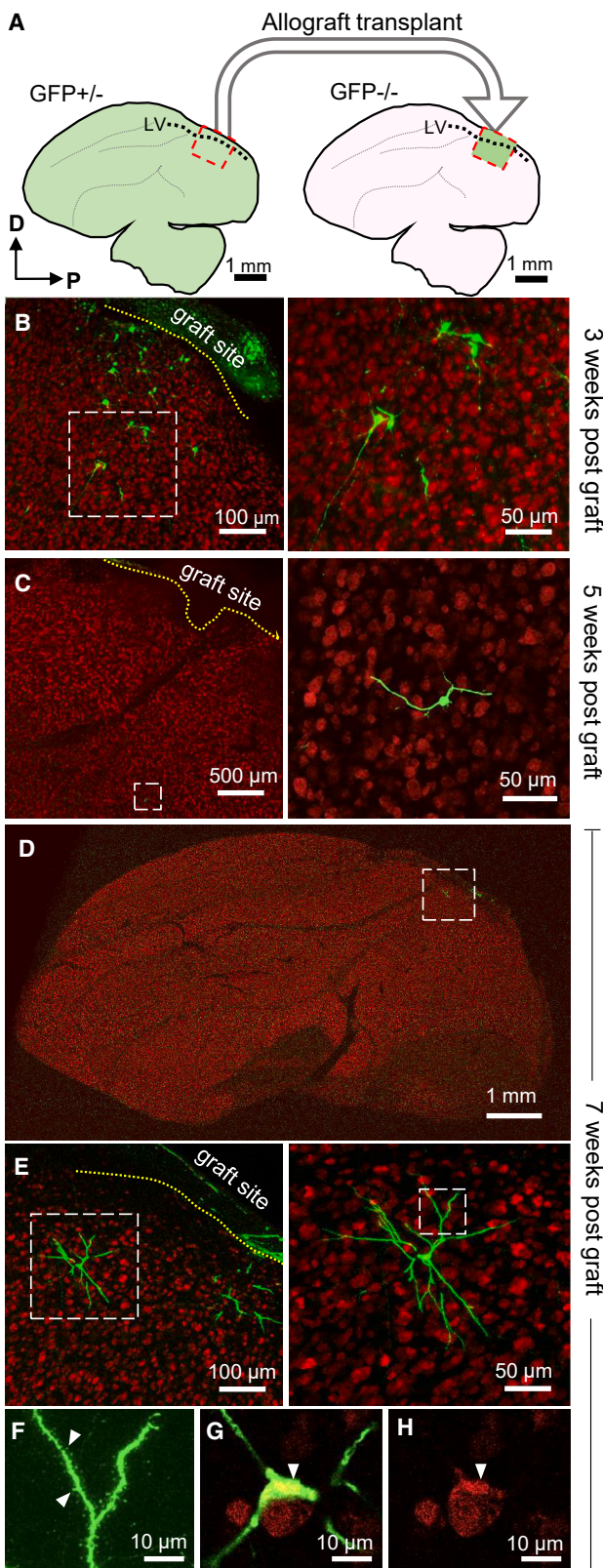


**Figure 2. GFP<sup>+</sup> cells from donor transplants migrate into host brains and become neurons**

- (A) Schematic of the graft procedure.
- (B) Histological section from the host brain 3 weeks after transplantation, showing GFP<sup>+</sup> cells (green) and NeuN<sup>+</sup> neurons (red). Left: a yellow dotted line indicates the graft-host interface. Right: magnification of the white dashed region shown on right, showing GFP<sup>+</sup> migrating cells.
- (C) Left: histological section showing a GFP<sup>+</sup> cell located approximately 1.5 mm from the graft boundary (dotted yellow line). Right: magnification of the white dashed region shown on the left.
- (D) Sagittal section with NeuN<sup>+</sup> neurons in red and GFP<sup>+</sup> transplanted cell in green. The white dashed region indicates the location of the cell shown in (E).
- (E) Left: histological section from the host brain 7 weeks after transplantation. Shown are GFP<sup>+</sup> mature neurons (green) and mature NeuN<sup>+</sup> neurons (red). The yellow dotted line indicates the graft-host interface. Right: magnification of the white dashed region shown on the left, showing a GFP<sup>+</sup> neuron.
- (F) Magnification of the dashed region on the right in (D). White arrowheads point to dendritic spines.
- (G) Magnification of the GFP<sup>+</sup> cell shown in (D) and (E). A white arrowhead points to the soma; a single z plane is shown.
- (H) A white arrowhead points to the NeuN<sup>+</sup> soma of the cell shown in (F); a single z plane is shown.

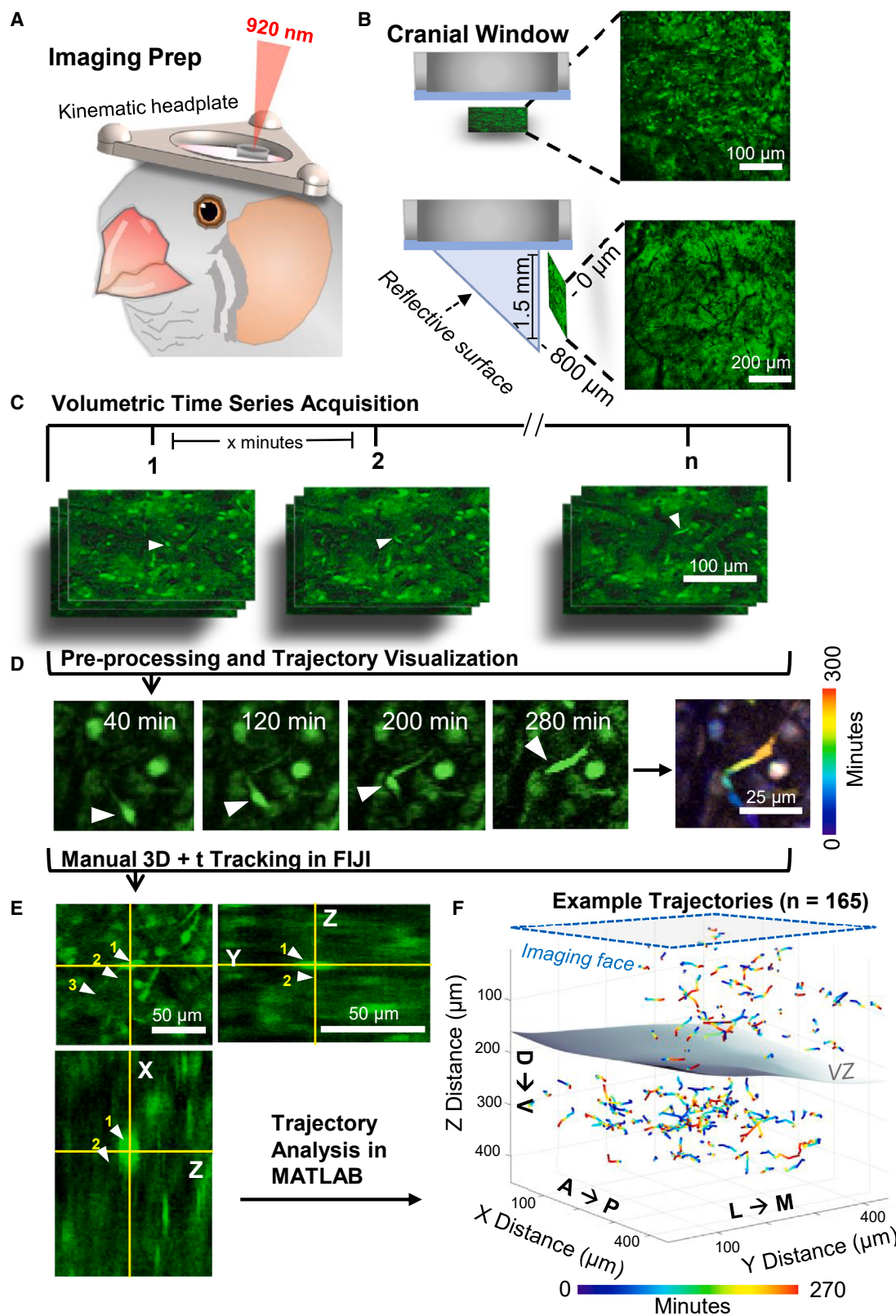
cells, many GFP<sup>+</sup>/DCX<sup>+</sup> cells exhibited a bipolar morphology with a small, elongated soma or were multipolar with a larger soma (Figure 1C), indicative of migratory neurons at different stages of maturity.<sup>15</sup>

Finally, we performed FISH against probes for glia. 8% of GFP<sup>+</sup> cells expressed platelet-derived growth factor receptor alpha (PDGFRA), which is enriched in oligodendrocyte precursor cells (OPCs; n = 50/594 cells). 3.27% of GFP<sup>+</sup> cells expressed CSF1R, a marker for microglia (3.27%, n = 8/245 cells), and 0% of GFP<sup>+</sup> cells expressed SLC15A2, a marker for astrocytes (n = 0/111 cells) (Table S1; Figure S2).

Together, these data indicate that, in the HVC and surrounding tissue of UBC-GFP transgenics, GFP appears to be primarily expressed in cells of a neurogenic lineage, including a high density of putative migratory neurons.

#### Transplanted GFP<sup>+</sup> cells migrate and become neurons in host brains

To further study the identity of GFP<sup>+</sup> cells in UBC-GFP birds, we transplanted a small piece of living brain tissue (5–10 mg) from transgenics into a wild-type hosts and then evaluated GFP expression in the host brain at different times post surgery (n = 6 birds; Figure 2A; Table S2). Three weeks after transplantation, GFP<sup>+</sup> cells were found in the host brain up to 350 μm from the edge of the graft. Some cells exhibited a bipolar morphology, characteristic of migratory neurons, and some expressed NeuN (n = 9/21 cells were NeuN<sup>+</sup>, 1 bird) (Figures 2B; Table S2). Five weeks after transplantation, GFP<sup>+</sup> cells were observed up to 2 mm from the graft and were commonly multipolar (average distance from the graft,  $1,042 \pm 626.23$  μm; n = 26 cells from 2 birds; Figure 2C). Seven to nine weeks post transplantation, GFP<sup>+</sup> cells that had dispersed into the host tissue now exhibited mature neuronal morphology, had spiny dendrites, and expressed NeuN (n = 9/9 cells, 3 birds; Figures 2D–H). These experiments indicate that the brains of UBC-GFP zebra finches contain GFP<sup>+</sup> cells that are capable of migrating into the brain of another animal and differentiating into mature neurons.



(legend on next page)

### **In vivo imaging in UBC-GFP songbirds reveals dynamic cell migration**

We next sought to determine whether GFP expression was bright and sparse enough to allow imaging of migrating cells *in vivo*. We implanted UBC-GFP birds with a 3-mm cranial window and kinematic headplate<sup>16</sup> and performed 2P time-lapse volumetric microscopy (Figures 3A–3C). Using this approach, we could resolve large numbers of individual cells down to 350 μm below the brain's surface. Many cells exhibiting the bipolar morphology characteristic of migratory neurons were found both above the VZ in the hyperpallium and below the VZ in regions of the nidopallium, including HVC (Figures 3B; Video S1). Time-lapse volumetric imaging through implanted cranial windows revealed a high density of GFP+ migratory cells throughout these regions that were moving in different directions and making frequent turns (Videos S2 and S3). To enable imaging of cells in deeper areas, we used a microprism approach, where a 1.5-mm microprism was bonded to a cranial window with optical adhesive and surgically implanted<sup>17–19</sup> (Figure 3B; STAR Methods). This microprism approach allowed imaging of cells up to 800 μm below the brain surface (Figures S4A and S4B). Using a combination of both cranial window and microprism approaches, we imaged migration in 8 birds (5 males, 3 females) for between 3 and 12 h and manually tracked 876 trajectories across all volumes (109.5 ± 44.6 trajectories per animal; Figures 3D–3F; Table S3).

We first evaluated dynamics of migratory cells in juvenile HVC (9–13 min per volume, 425 × 425 × 310 μm, n = 143 cells, 2 birds; Figure 4). HVC was retrogradely labeled through Dil injection into area X to enable localization of HVC under 2P excitation (Figure 4A). Migrating cells in HVC were dispersed throughout the imaging field of view (FOV) and moved in all directions (Figures 4C–4E). We did not detect a bias for a particular direction in the horizontal plane (Rayleigh's test, p = 0.83, n = 143 cells, 2 birds; Figure 4F). These cells also made frequent turns (mean tortuosity = 1.83 ± 0.69; Figure 4H) and moved along their path at speeds ranging from 7.0 to 45 μm/h (mean 14.65 ± 5.29 μm/h; Figure 4G). These dynamics were similar to those of retrovirally labeled migratory neurons in the juvenile songbird HVC.<sup>11</sup>

Similar dynamics were observed in the brains of adult birds 86–800+ days post hatch (dph; 3 males, 3 females, n = 594 cells). Both within HVC and in other regions of the nidopallium, we observed a large number of migrating cells that were distributed throughout the tissue and dispersing in all directions while making turns (Videos S2 and S3). Interestingly, cells in superficial regions (within 400 μm of the surface) exhibited a slight but statistically significant ventral bias (1.22 μm/h ventrally; t test, p < 0.005; n = 115 cells, 3 birds; Figures S4C–S4E), while deeper cells (over 400 μm from the surface) exhibited no ventral bias (t

test, p = 0.134; n = 133 cells, 3 birds). In addition, deeper cells had a significantly higher tortuosity than superficial cells (two-sample t test, p < 0.0005; Figure S4G).

We found no significant differences between the cells of juveniles (<89 dph, n = 282 cells) and adults (>89 dph, n = 248 cells) in speed (Mann-Whitney U test, p = 0.53) or tortuosity (Mann-Whitney U test, p = 0.34). Tortuosities in male birds (2.18 ± 1.05, n = 162 cells) were significantly higher than tortuosities in the females (1.43 ± 0.71, n = 298 cells) (Mann-Whitney U test, p < 0.01). There was no significant difference between female and male neuronal speeds (Mann-Whitney U test, p = 0.82).

Together, these results suggest the presence of a high density of migratory neurons in the brains of juvenile, adult, male, and female zebra finches.

### **Population analysis reveals an autonomous, disordered migration process**

We next wondered whether the migration dynamics of nearby cells were synchronized or whether cells moved in an independent fashion. We evaluated the correlation in heading direction and speed between 26,642 pairs of cells across 4 birds (105 ± 44 simultaneously recorded cells per bird). We did not observe a significant correlation in heading directions between pairs of cells (Figures 5A and 5B) (2-sample Kolmogorov-Smirnov test, p = 0.12). However, we did observe a small but significant correlation in the speed of cell migration between pairs of cells (p > 0.001) (Figure 5C). This correlation in speed was slightly inversely correlated with the distance between the pairs of cells (Figure 5D).

Next, to detect and evaluate the presence of ordered patterns in the movements of cells, we estimated the Shannon entropy of migration dynamics (Figures 5E and 5F; STAR Methods). We found that the entropy of the position and heading of cells were well fit by a uniform random distribution maximum entropy model across a range of spatial scales (Figures 5G and 5H). Together, these results suggest that migration in the postnatal zebra finch forebrain is consistent with a disordered process in which cells show little correlation in their positions, heading, and speed.

### **Migrating neurons may flexibly use vascular scaffolds**

We investigated whether the migrating neurons may rely on migratory scaffolds during their migration as evaluated in previous work.<sup>7,20–25</sup> Consistent with previous studies, we found few vimentin-positive (Vim+) fibers in HVC relative to other regions of the zebra finch brain (Figure S6). In histological sections, we found only a few cases of cells with migratory morphology associated with Vim+ fibers in HVC and surrounding nidopallium (4/22 cells, n = 1 bird) (Figure S6D). This is consistent with

**Figure 3. Migratory GFP+ cells can be imaged in UBC-GFP birds using 2P microscopy**

- (A) Imaging preparation. The kinematic headplate and optical implant are shown. A 920-nm light beam is shown entering the optical implant.
- (B) Top: cranial window implant schematic and example FOV. Bottom: microprism implant schematic and example FOV.
- (C) Design for 2P volumetric time-lapse recordings.
- (D) Visualization of a single migrating cell (white arrowheads) over time.
- (E) Schematic of manual tracking in 3D over time, performed in FIJI using a custom plug-in, for a single cell. White arrowheads and yellow numbers indicate positions of the cell's soma at future time points.
- (F) Example tracked trajectories, temporally color coded from a single juvenile animal both above and below the VZ, as depicted by a schematized layer in gray.

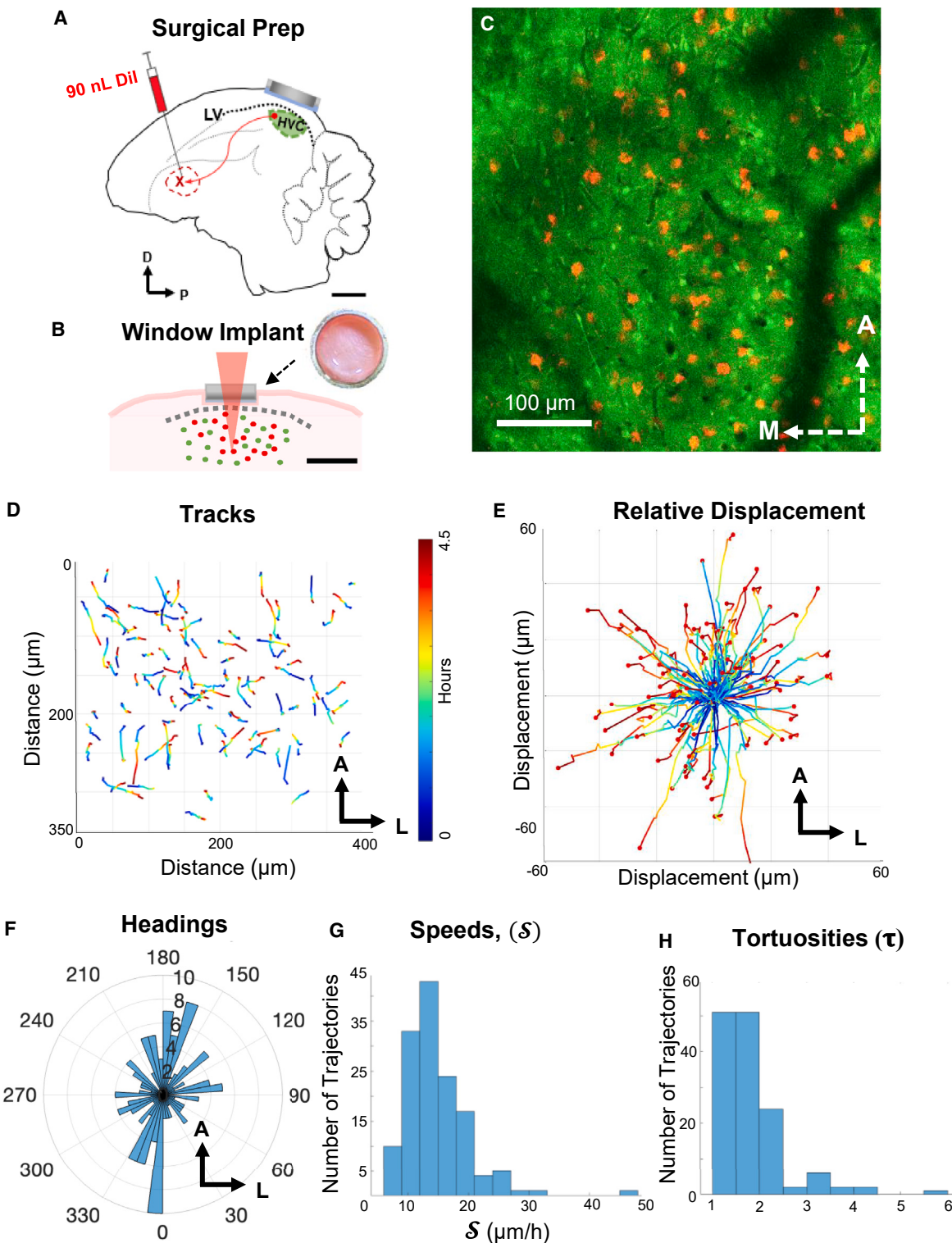


**Figure 4. Dynamics of neuroblast migration in male zebra finch HVC**

(A) Surgical preparation of a zebra finch for HVC imaging, retrograde injection of Dil into area X, and cranial window placement over HVC coordinates. Scale bar, 1 mm.

(B) Schematic of the cranial window implant, with 2P stimulation (920 nm) of Dil+ cells shown in red. Scale bar, 3 mm.

(C) 2P microscopy image of a single plane in HVC showing GFP expression (green) and Dil+ HVC<sub>X</sub> cells (red).

(legend continued on next page)

previous studies that have suggested that migrating neurons in HVC may not be dependent on Vim+ fibers for migration.<sup>7,10,11</sup>

To evaluate association with vasculature, we labeled the vasculature with SR-101 at the end of *in vivo* imaging sessions and compared the migratory trajectories with the pattern of blood vessels ( $n = 115$  cells,  $n = 2$  birds) (Figure S5; Video S4). Over a 3-h imaging session, 21% of cells exhibited trajectories that closely aligned with the path of the vasculature ( $n = 17/81$  cells, 1 bird; STAR Methods). Interestingly, we observed that the majority of vasculature-associated cells (64.7%,  $n = 11/17$  cells) did not follow the path of the vessel for the entirety of their trajectories. Instead, they appeared to hop on the vasculature for a portion of their trajectory and then hop off again. These cells followed vasculature for an average of  $35.17 \pm 21.02 \mu\text{m}$  out of their total  $48.64 \pm 17.06\text{-}\mu\text{m}$ -long trajectories (71.8% of total path traveled spent on vasculature, on average). Cells that followed vasculature at some point during their trajectory were significantly faster on average than cells that were not associated with vasculature at all ( $15.55 \pm 17.90 \text{ vs. } 10.81 \pm 13.36 \mu\text{m/h}$ ) (two-sample t test,  $p < 0.001$ ).

Similar results were observed across a longer imaging session (11.43 h, 63 cells, 1 bird). The paths of a small number of cells (28.6%,  $n = 18/63$  tracks) aligned with the paths of the SR-101-labeled vasculature for some segment of their trajectory. Nearly all of the migratory cells that followed along vasculature paths did so transiently within the imaging session (17/18 trajectories; Figures S5B and S5C). These cells followed vasculature for an average of  $44.38 \pm 36.12 \mu\text{m}$  of their total  $86.49 \pm 37.19\text{-}\mu\text{m}$ -long trajectories (~51.3% of total path on average). Cells that followed vasculature at some point during their trajectory were significantly faster on average than cells that were not associated with vasculature at all (mean instantaneous velocity,  $8.03 \pm 7.80 \mu\text{m/h}$  vs.  $5.71 \pm 6.14 \mu\text{m/h}$ ; two-sample t test,  $p = 0.002$ ). These results suggest that some migrating neurons in the postnatal zebra finch brain may use vasculature for a portion of their migration path.

### Neuron migration is well described by a superdiffusive model

Our observations suggest that new neurons in the postnatal songbird brain disperse in various directions, make frequent turns, and are largely uncorrelated in their migration patterns. Therefore, we wondered whether their migratory behavior could be described by a diffusive model, similar to those applied to other migratory cell types, such as bacteria, mammalian T cells, and “super-spreading” cancer cells.<sup>26–28</sup> Quantitative analysis of diffusion in a system can offer insight into the biological mechanisms governing the migration of cell populations.<sup>29,30</sup> To evaluate a diffusive model of migration, we computed the mean squared displacement (MSD) of the soma centroid over time from tracked cells (Figure 6). MSD for a single trajectory was computed using the following formula:

$$MSD = \langle \Delta r^2(\tau) \rangle = \langle |r(t+\tau) - r(t)|^2 \rangle_t$$

Where  $r(t)$  is the soma position at time  $t$ , and  $r(t + \tau)$  was the new soma position at time  $t + \tau$ .<sup>31</sup>

Next, we fit the displacement as a function of time using the formula  $MSD = \beta \tau^\alpha$ , where  $\beta$  (diffusion coefficient) and  $\alpha$  (scaling factor) are free parameters. The value of  $\alpha$  distinguishes different forms of diffusion, such as random walk ( $\alpha = 1$ ), ballistic motion ( $\alpha = 2$ ), or superdiffusion ( $1 < \alpha < 2$ )<sup>32–34</sup> (Figures 6A and 6B). This diffusion model was a good fit for migration of individual cells ( $75.7\%$  with  $R^2 > 0.95$ ) as well as the population average ( $R^2 > 0.98$  overall). We examined how  $\alpha$  varied across trajectories from different animals and brain regions. All regions were well fit by  $\alpha$  ranging from 1.4 to 1.6 in HVC and 1.3 to 1.8 across different regions ( $n = 8$  birds,  $R^2 > 0.99$ ) (Figures 6C and 6D; Table S4).

We fit the diffusion model to all individual cells tracked from these experiments ( $n = 876$  trajectories, 8 birds) (Figures 6E and 6F). The distribution of  $\alpha$  values from individual cells ( $n = 663$  with  $R^2 > 0.95$  of 876 trajectories) formed a unimodal distribution that had an average  $\alpha = 1.77 \pm 0.5$  (Figure 6F). This is consistent with a model where all cells obey the same migratory mechanism, as opposed to a model in where two separate populations of cells follow separate mechanisms. Superficial cells ( $n = 94$  cells) and deeper cells ( $n = 85$  cells) did not differ significantly in their  $\alpha$  parameters (two sample t test,  $p = 0.61$ ) (Figure 6G), and we found no significant relationship between the  $\alpha$  of individual cells and the average depth of their tracked trajectory (using a linear regression test,  $p = 0.53$ ,  $n = 179$  cells), with no correlation with Pearson’s correlation coefficient ( $R = 0.05$ ) (Figure 6H). We also found no significant difference between good  $\alpha$  fits of juveniles and adult cells (Mann-Whitney U test,  $p = 0.24$ ,  $n = 227$  juvenile cells, 178 adult cells) or between female and male cells (Mann-Whitney U test,  $p = 0.39$ ,  $n = 231$  female cells, 93 male cells). We did not find any significant relationship between the  $\beta$  parameter and the age, sex, brain region, or imaging time of the animal. Together, these results suggest that superdiffusion persists across different depths, brain regions, and ages across both individual cells and the average population dynamics.

### Simulating neuron migration in a virtual songbird brain

The results so far suggest that new neurons in the adult songbird HVC engage in a diffusion-like migration process. We designed a generative model of migration to evaluate whether this process is sufficient to allow neurons to disperse to integration targets in and around HVC over 3–4 weeks, which is the timescale for migration reported in previous studies.<sup>7</sup> In our model, simulated cells were born at random positions across a 2D plane representing the VZ (STAR Methods). After birth (at time  $t = 0$ ), cells migrate throughout a 3D volume in steps corresponding to

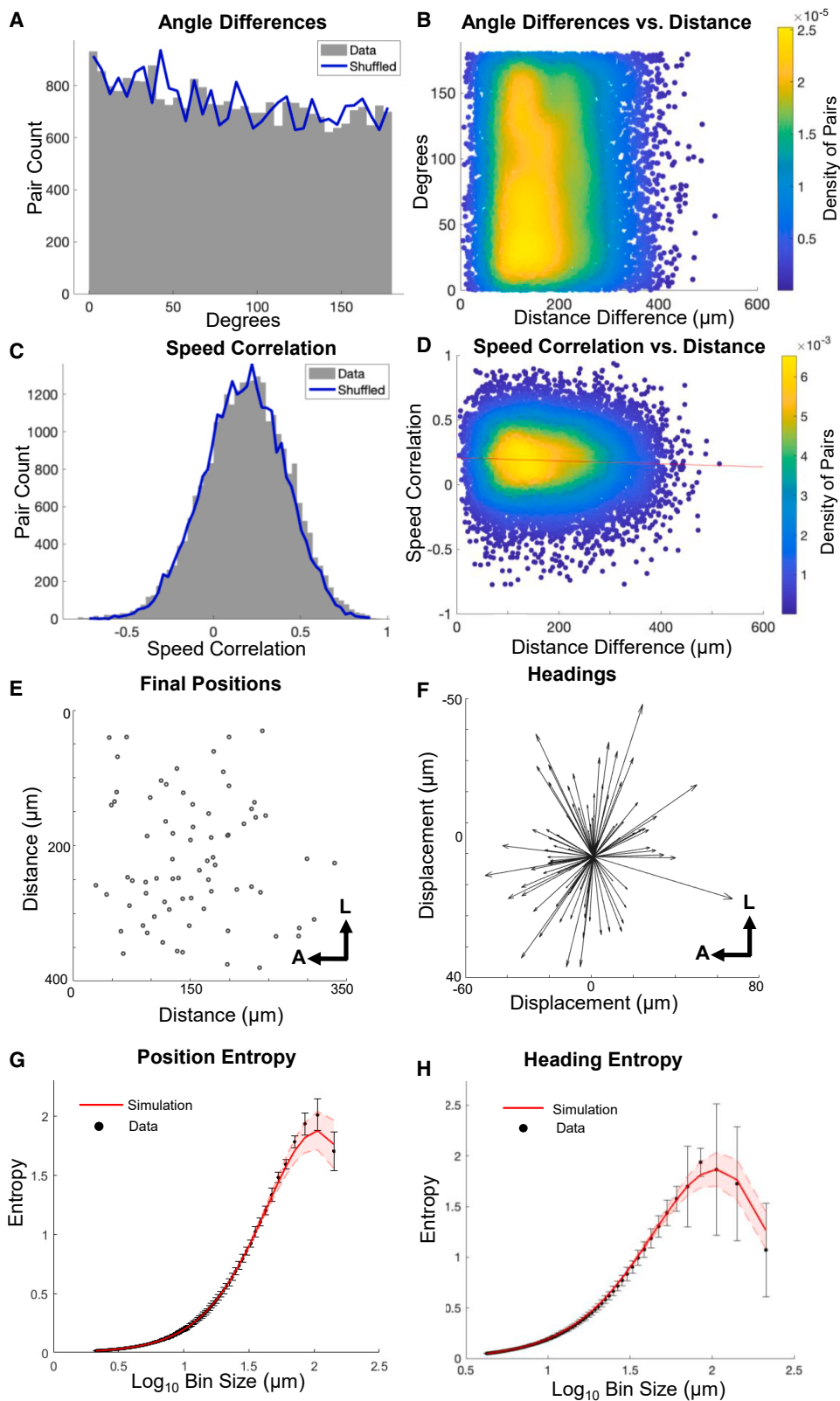
(D) Tracked trajectories of 96 migrating cells. Color indicates the time within the 4.5 h duration imaging session.

(E) Relative displacement of cells shown in (D) with normalized start positions.

(F) Histogram of cell heading angles in the horizontal plane (Rayleigh’s test,  $p = 0.83$ ;  $n = 143$  cells,  $n = 2$  birds).

(G) Distribution of average speeds of migrating cells ( $n = 143$  trajectories,  $n = 2$  birds). Mean speed =  $14.65 \pm 5.29 \mu\text{m/h}$ .

(H) Distribution of tortuosities of migrating cells ( $n = 143$  trajectories,  $n = 2$  birds). Mean tortuosity =  $1.83 \pm 0.69$ .



(legend on next page)

10 minutes of real-world time. At each step, their position ( $P_t$ ) is updated by the following formula:

$$P_t = P_{t-1} + d * H_t$$

where  $P_{t-1}$  is its position at the preceding time point,  $H_t$  is the cell's heading for the current step, and  $d$  is the magnitude of the step being taken (Figures 7A and 7B). At each time point, the value of  $d$  was drawn from an experimentally derived distribution (Figure S7A). To reflect the changes in direction that cells exhibit during migration, the cells heading,  $H_t$ , is constructed using the following algorithms:

$$Hx, t = \sin(AXY, t + \Delta a) * \cos(AXZ, t + \Delta a)$$

$$Hy, t = \cos(AXY, t + \Delta a) * \cos(AXZ, t + \Delta a)$$

$$Hz, t = \sin(AXZ, t + \Delta a)$$

where  $A$  represents the angle direction in which a cell is currently heading in xy or xz, and  $\Delta a$  is the change in heading angle (Figure 7A). The value of  $a$  was drawn stochastically at each time step  $t$  from distributions derived from experimental data (Figure S7B).

These simulated neurons exhibited migratory dynamics similar to cells observed *in vivo* ( $n = 143$  cells across 2 birds, 3 h of migration divided into 10-min intervals). When measured across 3 h, the paths of simulated cells had similar tortuosities compared with *in vivo* cells and were well fit by a diffusive model with similar  $\alpha$  parameters ( $\mu_{\text{sim}} = 1.5539 \pm 0.0076$ ,  $\mu_{\text{track}} = 1.5595$ ), indicating that the simulation was able to generate similar migration patterns compared with real cells (Figures S7E–S7G; STAR Methods). Populations of simulated cells also exhibited a similar level of disorder compared with tracked cells. The entropy of both the position and headings of simulated cells was similar to tracked cells ( $n = 96$  cells, percent error<sub>position</sub> = 4.69%, percent error<sub>heading</sub> = 1.38%) (Figures 7E–7J). Altogether, these results suggest that this simulation recapitulates several key features of new neuron migration in the postnatal zebra finch brain.

We next simulated the migration of 1,000 new neurons in HVC over multiple weeks (Figure 7C). After 21 days, simulated cells were found throughout HVC and the surrounding tissue up to  $1.580 \pm 0.065$  mm from the VZ. The population center of mass (COM) was located  $373.33 \pm 3.07$   $\mu\text{m}$  from the VZ, which is similar to the distance from the VZ to the center of HVC *in vivo* (374.35  $\mu\text{m}$ ).<sup>35</sup> At the end of 40 days, simulated cells had dispersed further, migrating up to  $2.16 \pm 0.345$  mm from the VZ with a COM of  $536.4 \pm 10.46$   $\mu\text{m}$  from the VZ (Figure 7D). These data suggest that this form of migration is sufficient to distribute cells throughout HVC and beyond over the biologically relevant timescale for migration and integration.

## DISCUSSION

Here we evaluated UBC-GFP zebra finches, a previously developed transgenic zebra finch line,<sup>12</sup> for the study of neuron migration and provided an in-depth quantitative characterization of neuron migration in the postnatal zebra finch brain. We found that migratory cells are present throughout HVC and surrounding tissue at high density, disperse in all directions, and may use vasculature as migratory scaffolding. We show that these dynamics can be modeled as a superdiffusive process. Furthermore, this type of neuron migration is sufficient to populate HVC *in silico*. Together, these results reveal a form of superdiffusive migration that underlies new neuron dispersion in the juvenile and adult brain.

## Comparison with other forms of migration

Previous work in songbirds has predicted the existence of diffusion-like migration in and around HVC. Vellema et al.<sup>36</sup> used mathematical modeling of the positions of newborn bromodeoxyuridine (BrdU)-labeled cells to predict a “random migration” that could explain patterns of cell dispersal in the canary brain.<sup>36</sup> This diffusion-like migration was also supported by *in vivo* imaging of retrovirally labeled newborn neurons in zebra finches in the anesthetized, juvenile HVC song nucleus.<sup>11</sup> In the present study, we provide additional evidence to support this prediction through detailed quantitative characteristics of hundreds of new neurons. We also show that this form of diffusion-like

## Figure 5. Population analysis reveals an autonomous, disordered migration process

- (A) Distribution of angle differences between the trajectories of 26,642 pairs of cells (gray) from 4 birds (3 males, 1 female) compared with shuffled data (blue line) (2-sample Kolmogorov-Smirnov test,  $p = 0.12$ ).
- (B) Scatterplot of pairwise angle differences and distance difference between the cell pair. Each point represents a cell pair, and color indicates kernel density estimate. There was no significant relationship between angle difference and distance between pairs (linear regression,  $p = 0.9$ ).
- (C) Distribution of speed correlations (Spearman's) between the trajectories of 26,642 pairs from 4 birds (3 males, 1 female) compared with shuffled-data pairwise speed correlations (2-sample Kolmogorov-Smirnov test,  $p < 0.0005$ ).
- (D) A small but significant relationship was found between speed correlation and distance between pairs (linear regression, slope =  $-0.000118$  change in correlation value per micron,  $p < 0.0005$ ,  $R^2 = 0.0018$ ). This effect was slightly greater than expected by shuffled data (linear regression, slope =  $-8.0685e-05$  change in correlation value per micron,  $p < 0.0005$ ,  $R^2 = 0.000935$ ).
- (E) Positions of 96 simultaneously recorded migratory cells in the imaging volume, projected into a single plane.
- (F) Headings of 96 simultaneously recorded migratory cells in the imaging volume.
- (G) Entropy average of observed cell positions across time (black dots), plotted with a mean of 1,000 simulations of the maximum entropy model run with the mean number of position observations across time (red line). Black error bars indicate the standard deviations of entropies of 96 cells' positions across 18 time points within 4.5 h. The shaded red region indicates the standard deviation of entropy across 1,000 simulations.
- (H) Entropy of trajectory directions across a 4.5-h imaging session (black dots). Black error bars indicate the standard deviations of entropies of 96 cells' cumulative heading directions across 17 time points within 4.5 h. The red line indicates the mean of 1,000 simulations of the maximum entropy model, and the shaded red region is the standard deviation of entropy across 1,000 simulations.

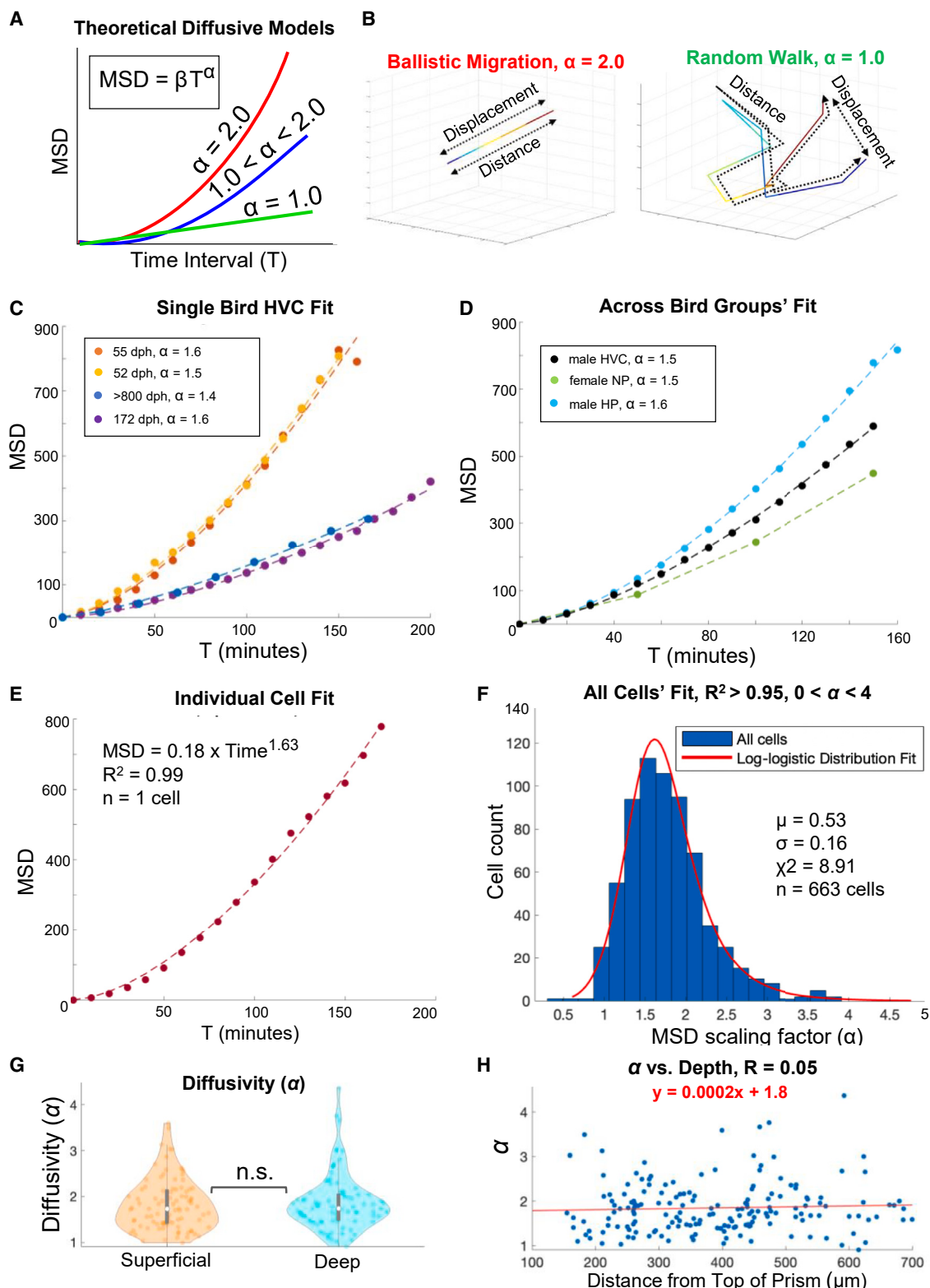


**Figure 6. Migration dynamics are well fit by a superdiffusive model**

(A) Schematic indicating the MSD vs. time (T) power law model and relevant  $\alpha$  parameters under different diffusion types: ballistic (red), superdiffusive (blue), and random walk (green).

(legend continued on next page)

migration extends beyond the boundaries of HVC and that it persists well into adulthood in both males and females.

Diffusion-like migration has also been observed in other neural systems but not at the spatiotemporal scale we describe. For example, in the developing cortex, before, during, or after cells' association with radial glia, new pyramidal neurons may exhibit diffusion-like movements.<sup>37–39</sup> It has also been observed in *ex vivo* time-lapse experiments that tangentially migrating interneurons undergo random-walk-like movements in the developing cortex, not dissimilar to the migration that we describe here.<sup>40,41</sup> Furthermore, *in vivo* time-lapse experiments showed that migratory interneurons with bipolar morphology move in many different directions in the intact developing cortex.<sup>42,43</sup> These tangentially migrating interneurons do not seem to be dependent on radial glial scaffolds but instead may be able to switch their migratory strategy between scaffold-associated and scaffold-free migration, especially when they arrive at the cortex.<sup>20,44–47</sup> Finally, in the adult rostral migratory stream (RMS), a major route for newborn neurons in the adult mammalian brain, time-lapse experiments showed that almost a third of migration cells exhibited local, “exploratory” dynamics and changed direction frequently.<sup>48,49</sup>

However, there are key differences between these previously described forms of diffusion-like migration and what we describe here. The first key difference is that, in the developing cortex and the adult RMS, diffusion-like migratory dynamics are more restricted in space and time than in the songbirds. Among radially migrating projection neurons in the mammalian cortex, the diffusion-like migration occurs at a brief phase of migration within the subventricular zone that lasts about 24 h, prior to the resumption of radial migration.<sup>38,39,50</sup> In tangentially migrating neurons, diffusion-like dynamics are likely restricted to either the marginal zone or subventricular zone/intermediate zone layers, where “multidirectional migration” occurs, before the postnatal invasion of the cortical plate radially.<sup>42,43,51,52</sup> Last, the migratory neurons of the RMS are spatially confined to a narrow band in the ventral forebrain unless there is nearby tissue damage.<sup>21,53,54</sup>

A second key difference is that all of these other streams of migration are highly directed. Radially migrating cells' trajectories are oriented perpendicular to the VZ, tangentially migrating neurons migrate hundreds of micrometers parallel to the VZ before switching to radial migration in the cortex, and, in the case of the RMS, migration is directed toward the olfactory bulb.<sup>50,53,55</sup> Thus, the diffusion-like patterns observed in time-lapse experiments from these systems appear to be relatively small deviations from an overall directed pattern of migration.

It is unclear why the form of neuron migration we observe differs from migration in these other systems. One possibility is that differences in experimental or analytical methods may accentuate the differences in migration patterns across these systems. Perhaps future quantitative analyses comparing large numbers of migratory neurons across these systems *in vivo* will reveal more similarities. Another possibility is that diffusion-like migration is more prominent in non-laminar structures, such as brain nuclei, and less prominent in laminar structures, such as the neocortex. Perhaps further analysis of neuron migration in the development of nuclear structure in the mammal will reveal more widespread diffusion-like patterns. Interestingly, recent work in amygdala tissue of adult humans discovered the existence of immature neurons with embryonic origins that may also migrate in an undirected manner.<sup>56</sup> Finally, it is possible that the form of migration we observe is a specialization of migration in the adult avian brain to facilitate the replacement of lost cells in a flexible and efficient manner.

### Superdiffusive migration may offer efficient dispersal

Superdiffusion has been observed across a range of motile biological systems, including intracellular molecular motors, super-spreading cancer cells, cerebellar migrating neurons, and predatory animals.<sup>28,57–59</sup> In these systems, superdiffusive dispersal dynamics have been proposed to be advantageous in sampling an environment with sparse cues. Whereas a random walk is prone to oversampling, and a more directed, ballistic strategy maximizes distance but undersamples, superdiffusion can be optimal.<sup>60–62</sup> For example, the superdiffusive searching behaviors of immunocyte T cells may enable the immune system to find and destroy rare targets more efficiently.<sup>26</sup> At the organismal level, superdiffusivity may play a role when prey is sparse and may offer predators, such as sharks, a flexible strategy to meet environmental demands.<sup>59</sup> Although the mechanisms giving rise to superdiffusion are not yet clear, perhaps superdiffusive migratory neurons in adult songbird brains are more efficient at sampling their local environment and finding targets like migratory cues or prime integration targets within the circuit.

Although, mathematically, superdiffusion implies a stochastic process, it is unclear whether new neurons make flexible decisions as they migrate or, alternatively, follow a predetermined but highly tortuous path. Within HVC, neurons were not observed to exclusively follow two well-described scaffolds in the embryonic and adult brain; namely, radial fibers and vasculature. However, we cannot rule out the possibility that cells migrate along radial fibers outside of HVC or follow Vim-negative fibers.

(B) Left: schematic of ballistic migration. Right: schematic of random walk migration.

(C) Diffusion model fit for the average 2D MSD of 301 migratory cells from four male HVCs (52 dph [n = 44], 55 dph [n = 95], 172 dph [n = 79], and >800 dph [n = 83]).

(D) Model fits to the average 2D MSD of cells in different brain regions. Male HVC data include 218 cells from 3 males, female nidopallium (NP) data include 247 cells from 2 female birds, and male hyperpallium (HP) data include 143 cells from 2 males.

(E) Model fit to an example cell's MSD.

(F) Histogram of the  $\alpha$  parameter distribution across all cells (n = 663/940 cells with  $R^2 > 0.95$ ,  $\alpha < 4$ ). The data are well fit by a unimodal log-logistic distribution (red line). The average  $\alpha$  is  $1.7664 \pm 0.5004$ .

(G) Violin plots of the MSD coefficient,  $\alpha$ , from superficial (n = 94) or deep cells (n = 85). There was no significant differences between groups (two-sample t test, p = 0.61, n = 3 birds).

(H) Scatterplot of  $\alpha$  plotted across different depths. No correlation was found between  $\alpha$  and depth (Pearson's correlation coefficient R = 0.05, n = 179 cells) with no significant linear relationship (p = 0.53).

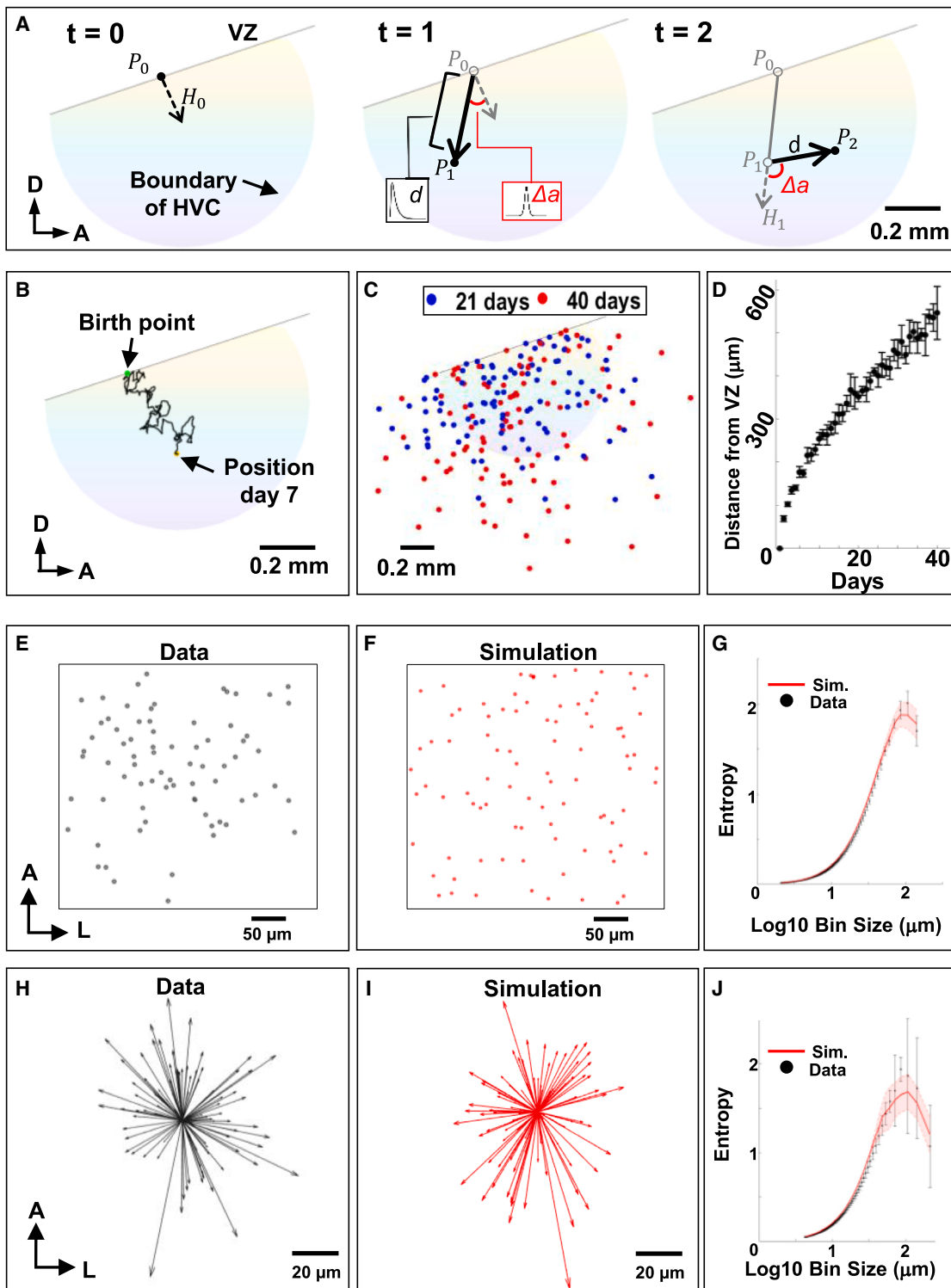


**Figure 7. Simulating neuron migration in a virtual songbird brain**

(A) Schematic of movement rules for a simulated neuron within virtual HVC. Left: at  $t = 0$ , a cell is born at a random position ( $P_0$ ) with a heading  $H_0$ . Center: at  $t = 1$ , step size  $d$  and change in heading  $\Delta a$  are randomly drawn from probability distributions. The cell's change in 3D position is calculated, and the cell moves to its new position ( $P_1$ ) with its new heading. Right: this process repeats itself, with  $d$  and  $\Delta a$  being drawn again and  $P_t$  being calculated until the user-specified duration is complete.

(legend continued on next page)

**Potential mechanisms of neuron migration in songbirds**

Although the precise mechanisms that guide neurons on their route through the zebra finch brain are unknown, there are several known molecular factors that control neuron migration in songbirds. For example, brain-derived neurotrophic factor (BDNF) is known to promote neuron migration in explant cultures from the canary brain.<sup>63</sup> In addition, the transition from expression of N-cadherin to NgCAM is thought to promote neuron migration in canaries.<sup>64</sup> Estrogen is thought to promote the departure of the cells from the VZ through an interaction with NgCAM in both zebra finch and canary explant cultures.<sup>65</sup> Studies *in vivo* show that the integration and survival of new neurons in HVC depends on testosterone, BDNF, and singing as well as the death of adult neurons.<sup>3,66,67</sup>

In addition to molecular cues, the physical properties of the tissue, including stiffness, density, and topology, can influence cell migration.<sup>68–70</sup> For example, the shape of micropillars in a dish dictate whether migratory neurons will migrate directionally or undergo local, exploratory movements.<sup>70</sup> We speculate that these physical factors may be important to consider in the adult zebra finch as the mature brain poses several physical challenges for migrating neurons that are not present during development, such as increased cellular density, modifications of the extracellular space, increased vascularization, and the presence of highly stable functional structures, such as synapses.<sup>8,71</sup> Recent studies provide a framework to understand how “molecular working memory” can allow migrating cells to maintain long-range migration trajectories despite local obstacles and noisy cue environments.<sup>72,73</sup> Thus, there are many potential mechanisms, both molecular and structural, that may contribute to the superdiffusive dynamics observed here in the adult songbird brain.

**Simulation predicts the existence of multiple forms of migration**

Using our large dataset of hundreds of *in vivo* trajectories, we developed a simulation of neuronal migration. Our simulation revealed that diffusion-like migration is sufficient to populate HVC and nearby regions with new neurons across biologically relevant timescales. This generative model is part of a growing class of quantitative models that simulate cellular dynamics and pattern formation in tissue development,<sup>74–78</sup> including neuronal migration.<sup>79–82</sup>

Our simulation also makes several testable predictions. For one, our model predicts that cells are not predetermined to integrate in a particular region. Instead, their integration location is determined by a series of stochastic choices along their path. Additionally, in this model, cells are not influenced by environmental factors. For example, cell death or tissue damage would not direct migration toward lesioned areas. Finally, even after 40 days, stochastic dynamics alone were insufficient to reach the long distances (5 mm) described in previous experiments.<sup>7</sup> Others have proposed that migration could be more directed, or more ballistic, in different parts of the avian brain. Work in canaries suggests that cells move more linearly in anterior regions of the brain,<sup>36</sup> and this could be a result of those brain regions being enriched with radial glia.<sup>7,36</sup> The presence of radial glial scaffolding would restrict the range of possible angles that cells’ trajectories could take, increasing the rate of dispersal. It is also possible that interactions with scaffolding actually increase migratory speeds rather than just restricting the range of possible turning angles. We report here that cells associated with vasculature may move more quickly than cells not associated with vasculature, indicating that, in other brain areas with different tissue architecture, migratory speeds may differ. This possibility motivates imaging studies in other brain regions.

**Experimental outlook for UBC-GFP songbirds**

UBC-GFP zebra finches enable imaging of large populations of migrating neurons *in vivo* without the need for viral labeling. The widespread expression of GFP could allow *in vivo* imaging in other regions of the brain with limited changes to the surgical preparation in future studies. Using 2P microscopy through a cranial window, we have been able to image migration 350 μm below the surface. However, three-photon microscopy can reach up to 1.3 mm *in vivo*.<sup>83</sup> This technology, in conjunction with UBC-GFP birds, could be used to image deeper regions of the zebra finch brain without the need for microprism implantation.

UBC-GFP songbirds could be also used to study the relationship between the birthplace of cells and their final integration site in the songbird brain. Previous studies of songbirds have proposed that the birthplace along the VZ determines the specific cell identity and integration site of newborn neurons.<sup>4</sup> Brain grafting experiments between UBC-GFP birds and wild-type birds could be used to test this hypothesis.

- 
- (B) Example path of a simulated cell over 7 days of migration. The cell begins its migration from a point (green dot) on the VZ (black line) and travels for 7 days before reaching its current position (yellow dot). Cells move in 3D, but only movements in the sagittal plane are shown.
- (C) Visualization of the positions of 100 simulated cells over 21 days (blue dots) and 40 days (red dots) of migration.
- (D) Plot showing the average distance from the ventricle of 1,000 simulated cells on each day of a 40-day simulation. Average distances of the simulated population (black dots, n = 1,000) were recorded across 5 simulation runs (error bars).
- (E) Positions of 96 migratory cells, simultaneously recorded *in vivo*, projected into a single plane.
- (F) Positions of 96 simulated migratory cells after 21 days of migration projected into a single 2D plane matching the dimensions of the imaging FOV shown in (E).
- (G) Entropy of cell positions from 96 tracked cells (black dots) plotted alongside the entropy of simulated cell positions across time (red line) (n = 96 cells). Black error bars are the standard deviations of entropies of 96 tracked cells’ positions across 18 time points within 4.5 h. The shaded red region indicates the standard deviation of entropy of 96 simulated cells subsampled from 1,000 simulated cells.
- (H) Tracked cell headings in the horizontal plane, normalized to the same start positions (n = 96 cells). Headings are represented as vectors between the first and last recorded positions of the cell.
- (I) Simulated cell headings in a 2D plane, normalized to the same start positions (n = 96 cells). Headings were recorded after 21 days of migration.
- (J) Entropy of cell headings from 96 tracked cell headings (black dots) plotted alongside the entropy of simulated cell headings across time (red line) (n = 96 cells). Black error bars indicate the standard deviations of entropies of 96 cells’ cumulative heading directions across 17 time points within 4.5 h. The shaded red region is the standard deviation of the heading entropy of 96 simulated cells subsampled from 1,000 simulated cells.

### Limitations of the study

In the present study, we characterize the migration of GFP+ cells in the adult brain. Available evidence suggests that the majority of these cells were neurons; over 90% of GFP+ cells express markers for young and mature neurons, and in transplant experiments, all (9/9) GFP+ cells that migrated out of the graft expressed NeuN and had neuron morphology. However, not all GFP+ cells expressed neuronal markers. A small proportion (~10%) expressed markers for glia cells, including microglia and OPCs. Therefore, it is possible that, in our *in vivo* imaging experiments, we observed a mixed population of migratory cells, including neurons, and a small number of OPCs and microglia. Given this possibility, it is interesting that our single-cell analysis revealed a unimodal distribution of migratory characteristics across the population, indicating a shared migratory strategy across all cells. This raises the question as to whether multiple cell types could utilize this superdiffusive mode of migration in the zebra finch brain.

Inspired by the apparent undirected nature of their movements, we speculate that these cells may be flexibly switching between multiple substrates. However, several experimental constraints limit our ability to resolve interactions between new neurons and these potential substrates, including glia and vasculature. First, although the radial glial staining is scarce in HVC,<sup>7,10,11</sup> we cannot rule out the possibility that cells migrate along Vim-negative fibers or other non-radial-glia scaffolding. Second, although the paths of cells sometimes ran parallel to vasculature, we did not have the resolution to determine whether cells contacted vasculature during this maneuver. Therefore, although we speculate that cells may flexibly choose their path, the data in the present study are also consistent with a predetermined path for each cell that is scaffold dependent but highly tortuous. Nevertheless, our observation of diffusion-like dynamics sets constraints on the structure of this potential scaffold.

The diffusive model of migration we describe here is purely descriptive in the sense that it attempts to describe or replicate the observed paths of cells *in vivo*. In future studies, it would be useful to develop a model of migration that incorporates mechanistic features. Indeed, previous studies have identified several of the biological factors that regulate cell migration in the adult.<sup>3,63–67</sup> An interesting next step could be to use more complex models to evaluate the impact of tethered and secreted guidance cues and occasional vascular interactions with migratory neurons and how they may give way to superdiffusive dynamics. Advancements in large-scale volumetric electron microscopy<sup>84</sup> could provide a high-resolution understanding of brain structure, concretizing the extracellular space and identifying cellular interactions to generate a more mechanistic model of migration.

### Conclusion

By applying *in vivo* 2P microscopy in transgenic zebra finches, we quantitatively characterized a diffusion-like form of migration in the adult brain. Based on these data, we developed a generative model that makes testable, quantitative predictions. We speculate that this migratory strategy enables neurons to efficiently navigate through the complex environment of the mature

nervous system. Finally, our work demonstrates the value of UBC-GFP transgenic songbirds as a resource for future investigations of adult neurogenesis.

### STAR★METHODS

Detailed methods are provided in the online version of this paper and include the following:

- **KEY RESOURCES TABLE**
- **RESOURCE AVAILABILITY**
  - Lead contact
  - Materials availability
  - Data and code availability
- **EXPERIMENTAL MODEL AND STUDY PARTICIPANT DETAILS**
- **METHOD DETAILS**
  - Surgical procedures
  - Immunohistochemistry and characterization of GFP expression
  - Fluorescent *in situ* hybridization chain reaction (HCR-FISH)
  - Two-photon (2P) microscopy
- **QUANTIFICATION AND STATISTICAL ANALYSIS**
  - Image processing and data analysis
  - Statistical tests
  - Migration simulation
  - Validation of migration simulation against experimental data
  - Simulation extrapolation analysis
  - Estimation of angle and step size distributions
  - Calculating entropy

### SUPPLEMENTAL INFORMATION

Supplemental information can be found online at <https://doi.org/10.1016/j.celrep.2024.113759>.

### ACKNOWLEDGMENTS

We thank Timothy O’chy, Mimi Kao, Sinead O’Brien, Amber Hickey, and the Boston University Animal Science Center for support and maintenance of the finch colony. Jack Giblin, Martin Thunemann, Natalie Thunemann, Ryan Senne, Su Jin Kim, Amy Monasterio, Steve Ramirez, Noshin Nawar, Jeroen Eyckmans, Todd Blute, and Boston University Research and Computing Services provided equipment and technical support. We thank Young Ye for tracking assistance and help with the tracking pipeline. We thank Peien Lyu, Christa Rose, Jacqueline Wang, Simon Castonguay, Lauren Dang, and Margaret Seo for tracking assistance and Brian DePasquale, Mike Economo, Ian Davison, Gabe Ocker, Lei Tian, Yujia Xue, and Kylie Moore for useful conversations about data analysis. We give special thanks to the zebra finches for their invaluable contribution to this research. N.R.S. was supported by an NSF NRT fellowship. This project was supported by seed funding from the Boston University Neurophotonics Center.

### AUTHOR CONTRIBUTIONS

Conceptualization, N.R.S. and B.B.S.; resources, T.J.G.; data collection, N.R.S., T.D., S.A., and B.L.B.; modeling and analysis, N.R.S. and S.A.; writing – original draft, N.R.S.; writing – review & editing, N.R.S., S.A., T.D., and B.B.S.

**DECLARATION OF INTERESTS**

The authors declare no competing interests.

Received: August 9, 2023

Revised: December 1, 2023

Accepted: January 23, 2024

Published: February 11, 2024

**REFERENCES**

1. Goldman, S.A., and Nottebohm, F. (1983). Neuronal production, migration, and differentiation in a vocal control nucleus of the adult female canary brain. *Proc. Natl. Acad. Sci. USA* **80**, 2390–2394.
2. Alvarez-Buylla, A., Kirn, J.R., and Nottebohm, F. (1990). Birth of projection neurons in adult avian brain may be related to perceptual or motor learning. *Science* **249**, 1444–1446.
3. Scharff, C., Kirn, J.R., Grossman, M., Macklis, J.D., and Nottebohm, F. (2000). Targeted Neuronal Death Affects Neuronal Replacement and Vocal Behavior in Adult Songbirds. *Neuron* **25**, 481–492.
4. Scott, B.B., and Lois, C. (2007). Developmental origin and identity of song system neurons born during vocal learning in songbirds. *J. Comp. Neurol.* **502**, 202–214.
5. Aronowitz, J.V., Kirn, J.R., Pytte, C.L., and Aaron, G.B. (2022). DARPP-32 distinguishes a subset of adult-born neurons in zebra finch HVC. *J. Comp. Neurol.* **530**, 792–803. <https://doi.org/10.1002/cne.25245>.
6. Colquitt, B.M., Merullo, D.P., Konopka, G., Roberts, T.F., and Brainard, M.S. (2021). Cellular transcriptomics reveals evolutionary identities of songbird vocal circuits. *Science* **371**, eabd9704.
7. Alvarez-Buylla, A., and Nottebohm, F. (1988). Migration of young neurons in adult avian brain. *Nature* **335**, 353–354.
8. Götz, M., Nakafuku, M., and Petrik, D. (2016). Neurogenesis in the Developing and Adult Brain—Similarities and Key Differences. *Cold Spring Harbor Perspect. Biol.* **8**, a018853.
9. Goldman, S.A., Lemmon, V., and Chin, S.S. (1993). Migration of newly generated neurons upon ependymally derived radial guide cells in explant cultures of the adult songbird forebrain. *Glia* **8**, 150–160.
10. Alvarez-Buylla, A., Theelen, M., and Nottebohm, F. (1988). Mapping of radial glia and of a new cell type in adult canary brain. *J. Neurosci.* **8**, 2707–2712.
11. Scott, B.B., Gardner, T., Ji, N., Fee, M.S., and Lois, C. (2012). Wandering Neuronal Migration in the Postnatal Vertebrate Forebrain. *J. Neurosci.* **32**, 1436–1446.
12. Agate, R.J., Scott, B.B., Haripal, B., Lois, C., and Nottebohm, F. (2009). Transgenic songbirds offer an opportunity to develop a genetic model for vocal learning. *Proc. Natl. Acad. Sci. USA* **106**, 17963–17967.
13. Barami, K., Iversen, K., Furneaux, H., and Goldman, S.A. (1995). Hu protein as an early marker of neuronal phenotypic differentiation by subependymal zone cells of the adult songbird forebrain. *J. Neurobiol.* **28**, 82–101.
14. Mullen, R.J., Buck, C.R., and Smith, A.M. (1992). A neuronal specific nuclear protein in vertebrates. *Dev. Camb. Engl.* **116**, 201–211.
15. Balthazart, J., Boseret, G., Konkle, A.T.M., Hurley, L.L., and Ball, G.F. (2008). Doublecortin as a marker of adult neuroplasticity in the canary song control nucleus HVC. *Eur. J. Neurosci.* **27**, 801–817.
16. Kim, S.J., Slocum, A.H., and Scott, B.B. (2022). A miniature kinematic coupling device for mouse head fixation. *J. Neurosci. Methods* **372**, 109549.
17. Andermann, M.L., Gilfoy, N.B., Goldey, G.J., Sachdev, R.N.S., Wölfel, M., McCormick, D.A., Reid, R.C., and Levene, M.J. (2013). Chronic cellular imaging of entire cortical columns in awake mice using microprisms. *Neuron* **80**, 900–913. <https://doi.org/10.1016/j.neuron.2013.07.052>.
18. Low, R.J., Gu, Y., and Tank, D.W. (2014). Cellular resolution optical access to brain regions in fissures: Imaging medial prefrontal cortex and grid cells in entorhinal cortex. *Proc. Natl. Acad. Sci. USA* **111**, 18739–18744.
19. Gengatharan, A., Malvaut, S., Marymonchyk, A., Ghareghani, M., Snappyan, M., Fischer-Sternjak, J., Ninkovic, J., Götz, M., and Saghatelian, A. (2021). Adult neural stem cell activation in mice is regulated by the day/night cycle and intracellular calcium dynamics. *Cell* **184**, 709–722.e13.
20. Porter, D.D.L., Henry, S.N., Ahmed, S., Rizzo, A.L., Makhlouf, R., Gregg, C., and Morton, P.D. (2022). Neuroblast migration along cellular substrates in the developing porcine brain. *Stem Cell Rep.* **17**, 2097–2110.
21. Grade, S., Weng, Y.C., Snappyan, M., Kriz, J., Malva, J.O., and Saghatelian, A. (2013). Brain-Derived Neurotrophic Factor Promotes Vasculature-Associated Migration of Neuronal Precursors toward the Ischemic Striatum. *PLoS One* **8**, e55039.
22. Farin, A., Suzuki, S.O., Weiker, M., Goldman, J.E., Bruce, J.N., and Canoll, P. (2006). Transplanted glioma cells migrate and proliferate on host brain vasculature: a dynamic analysis. *Glia* **53**, 799–808.
23. Snappyan, M., Lemasson, M., Brill, M.S., Blais, M., Massouh, M., Ninkovic, J., Gravel, C., Berthod, F., Götz, M., Barker, P.A., et al. (2009). Vasculature Guides Migrating Neuronal Precursors in the Adult Mammalian Forebrain via Brain-Derived Neurotrophic Factor Signaling. *J. Neurosci.* **29**, 4172–4188.
24. Sun, G.J., Zhou, Y., Stadel, R.P., Moss, J., Yong, J.H.A., Ito, S., Kawasaki, N.K., Phan, A.T., Oh, J.H., Modak, N., et al. (2015). Tangential migration of neuronal precursors of glutamatergic neurons in the adult mammalian brain. *Proc. Natl. Acad. Sci. USA* **112**, 9484–9489.
25. Tabata, H., Sasaki, M., Agetsuma, M., Sano, H., Hirota, Y., Miyajima, M., Hayashi, K., Honda, T., Nishikawa, M., Inaguma, Y., et al. (2022). Erratic and blood vessel-guided migration of astrocyte progenitors in the cerebral cortex. *Nat. Commun.* **13**, 6571.
26. Harris, T.H., Banigan, E.J., Christian, D.A., Konradt, C., Tait Wojno, E.D., Norose, K., Wilson, E.H., John, B., Weninger, W., Luster, A.D., et al. (2012). Generalized Lévy walks and the role of chemokines in migration of effector CD8+ T cells. *Nature* **486**, 545–548.
27. Ariel, G., Rabani, A., Benisty, S., Partridge, J.D., Harshey, R.M., and Be'er, A. (2015). Swarming bacteria migrate by Lévy Walk. *Nat. Commun.* **6**, 8396.
28. Nousi, A., Søgaard, M.T., Audoin, M., and Jauffred, L. (2021). Single-cell tracking reveals super-spreading brain cancer cells with high persistence. *Biochem. Biophys. Rep.* **28**, 101120.
29. Cai, A.Q., Landman, K.A., and Hughes, B.D. (2006). Modelling Directional Guidance and Motility Regulation in Cell Migration. *Bull. Math. Biol.* **68**, 25–52.
30. Toscano, E., Sepe, L., Del Giudice, G., Tufano, R., and Paoletti, G. (2022). A three component model for superdiffusive motion effectively describes migration of eukaryotic cells moving freely or under a directional stimulus. *PLoS One* **17**, e0272259.
31. Gal, N., Lechtman-Goldstein, D., and Weihs, D. (2013). Particle tracking in living cells: a review of the mean square displacement method and beyond. *Rheol. Acta* **52**, 425–443.
32. Saxton, M.J. (1997). Single-particle tracking: the distribution of diffusion coefficients. *Biophys. J.* **72**, 1744–1753.
33. Weihs, D., Mason, T.G., and Teitell, M.A. (2006). Bio-Microrheology: A Frontier in Microrheology. *Biophys. J.* **91**, 4296–4305.
34. Metzler, R., Jeon, J.-H., Cherstvy, A.G., and Barkai, E. (2014). Anomalous diffusion models and their properties: non-stationarity, non-ergodicity, and ageing at the centenary of single particle tracking. *Phys. Chem. Chem. Phys.* **16**, 24128–24164.
35. Benezra, S.E., Narayanan, R.T., Egger, R., Oberlaender, M., and Long, M.A. (2018). Morphological characterization of HVC projection neurons in the zebra finch (*Taeniopygia guttata*). *J. Comp. Neurol.* **526**, 1673–1689.

36. Vellema, M., van der Linden, A., and Gahr, M. (2010). Area-specific migration and recruitment of new neurons in the adult songbird brain. *J. Comp. Neurol.* **518**, 1442–1459.
37. Fishell, G., Mason, C.A., and Hatten, M.E. (1993). Dispersion of neural progenitors within the germinal zones of the forebrain. *Nature* **362**, 636–638.
38. Tabata, H., and Nakajima, K. (2003). Multipolar Migration: The Third Mode of Radial Neuronal Migration in the Developing Cerebral Cortex. *J. Neurosci.* **23**, 9996–10001.
39. Noctor, S.C., Martínez-Cerdeño, V., Ivic, L., and Kriegstein, A.R. (2004). Cortical neurons arise in symmetric and asymmetric division zones and migrate through specific phases. *Nat. Neurosci.* **7**, 136–144.
40. Kakita, A., and Goldman, J.E. (1999). Patterns and Dynamics of SVZ Cell Migration in the Postnatal Forebrain: Monitoring Living Progenitors in Slice Preparations. *Neuron* **23**, 461–472.
41. Tanaka, D.H., Yanagida, M., Zhu, Y., Mikami, S., Nagasawa, T., Miyazaki, J.i., Yanagawa, Y., Obata, K., and Murakami, F. (2009). Random Walk Behavior of Migrating Cortical Interneurons in the Marginal Zone: Time-Lapse Analysis in Flat-Mount Cortex. *J. Neurosci.* **29**, 1300–1311.
42. Ang, E.S.B.C., Haydar, T.F., Gluncic, V., and Rakic, P. (2003). Four-dimensional migratory coordinates of GABAergic interneurons in the developing mouse cortex. *J. Neurosci.* **23**, 5805–5815.
43. Inada, H., Watanabe, M., Uchida, T., Ishibashi, H., Wake, H., Nemoto, T., Yanagawa, Y., Fukuda, A., and Nabekura, J. (2011). GABA Regulates the Multidirectional Tangential Migration of GABAergic Interneurons in Living Neonatal Mice. *PLoS One* **6**, e27048.
44. Métin, C., and Godement, P. (1996). The ganglionic eminence may be an intermediate target for corticofugal and thalamocortical axons. *J. Neurosci.* **16**, 3219–3235.
45. Métin, C., Denizot, J.P., and Ropert, N. (2000). Intermediate zone cells express calcium-permeable AMPA receptors and establish close contact with growing axons. *J. Neurosci.* **20**, 696–708.
46. Wichterle, H., Turnbull, D.H., Nery, S., Fishell, G., and Alvarez-Buylla, A. (2001). In utero fate mapping reveals distinct migratory pathways and fates of neurons born in the mammalian basal forebrain. *Dev. Camb. Engl.* **128**, 3759–3771.
47. Li, G., Adesnik, H., Li, J., Long, J., Nicoll, R.A., Rubenstein, J.L.R., and Pleasure, S.J. (2008). Regional Distribution of Cortical Interneurons and Development of Inhibitory Tone Are Regulated by Cxcl12/Cxcr4 Signaling. *J. Neurosci.* **28**, 1085–1098.
48. Nam, S.C., Kim, Y., Dryanovski, D., Walker, A., Goings, G., Woolfrey, K., Kang, S.S., Chu, C., Chenn, A., Erdelyi, F., et al. (2007). Dynamic features of postnatal subventricular zone cell motility: A two-photon time-lapse study. *J. Comp. Neurol.* **505**, 190–208.
49. Martinez-Molina, N., Kim, Y., Hockberger, P., and Szele, F.G. (2011). Rostral migratory stream neuroblasts turn and change directions in stereotypic patterns. *Cell Adhes. Migrat.* **5**, 83–95.
50. Rakic, P. (1972). Mode of cell migration to the superficial layers of fetal monkey neocortex. *J. Comp. Neurol.* **145**, 61–83.
51. Lavdas, A.A., Grigoriou, M., Pachnis, V., and Parnavelas, J.G. (1999). The Medial Ganglionic Eminence Gives Rise to a Population of Early Neurons in the Developing Cerebral Cortex. *J. Neurosci.* **19**, 7881–7888.
52. Miyoshi, G., and Fishell, G. (2011). GABAergic interneuron lineages selectively sort into specific cortical layers during early postnatal development. *Cerebr. Cortex* **21**, 845–852.
53. Lois, C., and Alvarez-Buylla, A. (1994). Long-distance neuronal migration in the adult mammalian brain. *Science* **264**, 1145–1148.
54. Peretto, P., Merighi, A., Fasolo, A., and Bonfanti, L. (1997). Glial tubes in the rostral migratory stream of the adult rat. *Brain Res. Bull.* **42**, 9–21.
55. Marín, O. (2013). Cellular and molecular mechanisms controlling the migration of neocortical interneurons. *Eur. J. Neurosci.* **38**, 2019–2029.
56. Sorrells, S.F., Paredes, M.F., Velmeshev, D., Herranz-Pérez, V., Sandoval, K., Mayer, S., Chang, E.F., Insaurt, R., Kriegstein, A.R., Rubenstein, J.L., et al. (2019). Immature excitatory neurons develop during adolescence in the human amygdala. *Nat. Commun.* **10**, 2748.
57. Olah, M.J., and Stefanovic, D. (2013). Superdiffusive transport by multivalent molecular walkers moving under load. *Phys. Rev. E* **87**, 062713.
58. Wefers, A.K., Haberlandt, C., Surchev, L., Steinhäuser, C., Jabs, R., and Schilling, K. (2018). Migration of Interneuron Precursors in the Nascent Cerebellar Cortex. *Cerebellum* **17**, 62–71.
59. Sims, D.W., Humphries, N.E., Bradford, R.W., and Bruce, B.D. (2012). Lévy flight and Brownian search patterns of a free-ranging predator reflect different prey field characteristics. *J. Anim. Ecol.* **81**, 432–442.
60. Lomholt, M.A., Tal, K., Metzler, R., and Joseph, K. (2008). Lévy strategies in intermittent search processes are advantageous. *Proc. Natl. Acad. Sci. USA* **105**, 11055–11059.
61. Bartumeus, F., Catalan, J., Fulco, U.L., Lyra, M.L., and Viswanathan, G.M. (2002). Optimizing the Encounter Rate in Biological Interactions: L'evy versus Brownian Strategies. *Phys. Rev. Lett.* **88**, 097901.
62. Bartumeus, F., Da Luz, M.G.E., Viswanathan, G.M., and Catalan, J. (2005). Animal Search Strategies: A Quantitative Random-Walk Analysis. *Ecology* **86**, 3078–3087.
63. Louissaint, A., Rao, S., Leventhal, C., and Goldman, S.A. (2002). Coordinated Interaction of Neurogenesis and Angiogenesis in the Adult Songbird Brain. *Neuron* **34**, 945–960.
64. Barami, K., Kirschenbaum, B., Lemmon, V., and Goldman, S.A. (1994). N-Cadherin and Ng-CAM/8D9 are involved serially in the migration of newly generated neurons into the adult songbird brain. *Neuron* **13**, 567–582.
65. Williams, S., Leventhal, C., Lemmon, V., Nedergaard, M., and Goldman, S.A. (1999). Estrogen Promotes the Initial Migration and Inception of NgCAM-Dependent Calcium-Signaling by New Neurons of the Adult Songbird Brain. *Mol. Cell. Neurosci.* **13**, 41–55.
66. Li, X.-C., Jarvis, E.D., Alvarez-Borda, B., Lim, D.A., and Nottebohm, F. (2000). A relationship between behavior, neurotrophin expression, and new neuron survival. *Proc. Natl. Acad. Sci. USA* **97**, 8584–8589.
67. Kirm, J.R., and Nottebohm, F. (1993). Direct evidence for loss and replacement of projection neurons in adult canary brain. *J. Neurosci.* **13**, 1654–1663.
68. Ng, M.R., Besser, A., Danuser, G., and Brugge, J.S. (2012). Substrate stiffness regulates cadherin-dependent collective migration through myosin-II contractility. *J. Cell Biol.* **199**, 545–563.
69. Bénichou, O., Bodrova, A., Chakraborty, D., Illien, P., Law, A., Mejía-Monasterio, C., Oshanin, G., and Voituriez, R. (2013). Geometry-Induced Superdiffusion in Driven Crowded Systems. *Phys. Rev. Lett.* **111**, 260601.
70. Leclech, C., Renner, M., Villard, C., and Métin, C. (2019). Topographical cues control the morphology and dynamics of migrating cortical interneurons. *Biomaterials* **214**, 119194.
71. Roberts, T.F., Tschida, K.A., Klein, M.E., and Mooney, R. (2010). Rapid spine stabilization and synaptic enhancement at the onset of behavioural learning. *Nature* **463**, 948–952.
72. Nandan, A., Das, A., Lott, R., and Koseska, A. (2022). Cells use molecular working memory to navigate in changing chemoattractant fields. *Elife* **11**, e76825. <https://doi.org/10.7554/eLife.76825>.
73. Skoge, M., Yue, H., Erickstad, M., Bae, A., Levine, H., Groisman, A., Loomis, W.F., and Rappel, W.J. (2014). Cellular memory in eukaryotic chemotaxis. *Proc. Natl. Acad. Sci. USA* **111**, 14448–14453. <https://doi.org/10.1073/pnas.1412197111>.
74. Song, A., Gauthier, J.L., Pillow, J.W., Tank, D.W., and Charles, A.S. (2021). Neural anatomy and optical microscopy (NAOMI) simulation for evaluating calcium imaging methods. *J. Neurosci. Methods* **358**, 109173.
75. Allen, R., Mouronval, A.-S., and Aubry, D. (2010). Simulation of multiple morphogenetic movements in the *Drosophila* embryo by a single 3D finite element model. *J. Mech. Behav. Biomed. Mater.* **3**, 313–323.
76. Storjohann, R., and Marcus, G.F. (2005). NeuroGene: integrated simulation of gene regulation, neural activity and neurodevelopment.

- Proceedings of the 2005 IEEE International Joint Conference on Neural Networks<sup>1</sup>, pp. 428–433.
- 77. Jacobson, A.G., and Gordon, R. (1976). Changes in the shape of the developing vertebrate nervous system analyzed experimentally, mathematically and by computer simulation. *J. Exp. Zool.* **197**, 191–246.
  - 78. Kerstjens, S., Michel, G., and Douglas, R.J. (2022). Constructive connectomics: How neuronal axons get from here to there using gene-expression maps derived from their family trees. *PLoS Comput. Biol.* **18**, e1010382.
  - 79. Setty, Y., Chen, C.C., Scerier, M., Skoblov, N., Kalamatianos, D., and Emmott, S. (2011). How neurons migrate: a dynamic in-silico model of neuronal migration in the developing cortex. *BMC Syst. Biol.* **5**, 154.
  - 80. Gupta, S., Patteson, A.E., and Schwarz, J.M. (2021). The role of vimentin-nuclear interactions in persistent cell motility through confined spaces. *New J. Phys.* **23**, 093042.
  - 81. Gomez, J., Holmes, N., Hansen, A., Adhikarla, V., Gutova, M., Rockne, R.C., and Cho, H. (2022). Mathematical modeling of therapeutic neural stem cell migration in mouse brain with and without brain tumors. *Math. Biosci. Eng.* **19**, 2592–2615.
  - 82. Acosta-Soba, D., Castro-González, C., Geribaldi-Doldán, N., Guillén-González, F., Núñez-Abades, P., Ortega-Román, N., Pérez-García, P., and Rodríguez-Calván, J.R. (2023). Mathematical Modelling of Neuroblast Chemotaxis Migration towards the Olfactory Bulb. Preprint at arXiv. <http://arxiv.org/abs/2211.06166>.
  - 83. Horton, N.G., Wang, K., Kobat, D., Clark, C.G., Wise, F.W., Schaffer, C.B., and Xu, C. (2013). In vivo three-photon microscopy of subcortical structures within an intact mouse brain. *Nat. Photonics* **7**, 205–209.
  - 84. Kornfeld, J., Benezra, S.E., Narayanan, R.T., Svara, F., Egger, R., Oberlaender, M., Denk, W., and Long, M.A. (2017). EM connectomics reveals axonal target variation in a sequence-generating network. *eLife* **6**, e24364. <https://doi.org/10.7554/eLife.24364>.
  - 85. Schindelin, J., Arganda-Carreras, I., Frise, E., Kaynig, V., Longair, M., Pietzsch, T., Preibisch, S., Rueden, C., Saalfeld, S., Schmid, B., et al. (2012). Fiji: an open-source platform for biological-image analysis. *Nat. Methods* **9**, 676–682.
  - 86. Francis, F., Koulakoff, A., Boucher, D., Chafey, P., Schaar, B., Vinet, M.C., Fricourt, G., McDonnell, N., Reiner, O., Kahn, A., et al. (1999). Doublecortin is a developmentally regulated, microtubule-associated protein expressed in migrating and differentiating neurons. *Neuron* **23**, 247–256.
  - 87. Gleeson, J.G., Lin, P.T., Flanagan, L.A., and Walsh, C.A. (1999). Doublecortin is a microtubule-associated protein and is expressed widely by migrating neurons. *Neuron* **23**, 257–271.
  - 88. Boseret, G., Ball, G.F., and Balthazart, J. (2007). The microtubule-associated protein doublecortin is broadly expressed in the telencephalon of adult canaries. *J. Chem. Neuroanat.* **33**, 140–154.
  - 89. Alvarez-buylla, A., Buskirk, D.R., and Nottebohm, F. (1987). Monoclonal antibody reveals radial glia in adult avian brain. *J. Comp. Neurol.* **264**, 159–170.
  - 90. Airey, D.C., Castillo-Juarez, H., Casella, G., Pollak, E.J., and DeVoogd, T.J. (2000). Variation in the volume of zebra finch song control nuclei is heritable: developmental and evolutionary implications. *Proc. Biol. Sci.* **267**, 2099–2104.

## STAR★METHODS

### KEY RESOURCES TABLE

REAGENT or RESOURCE	SOURCE	IDENTIFIER
<b>Antibodies</b>		
rabbit polyclonal anti-GFP ( <i>1:400 dilution</i> )	Millipore Sigma	RRID: AB_3080
mouse monoclonal anti-NeuN ( <i>1:500 dilution</i> )	Millipore Sigma	MAB377, clone A60; RRID: AB_2298772
mouse monoclonal anti-DCX ( <i>1:400 dilution</i> )	Santa Cruz Biotechnology	sc-271390 (E–6); RRID:AB_10610966
mouse monoclonal anti-Vimentin (40E-C-s) ( <i>1:10 dilution</i> )	Developmental Studies Hybridoma Bank	RRID: AB_528504
a mouse monoclonal anti-HuC/HuD ( <i>1:500 dilution</i> )	Thermo Fisher Scientific	A-21271; RRID:AB_221448
Alexa Fluor 488 conjugated goat anti-rabbit ( <i>1:500 or 1:1000 dilution</i> )	Abcam	AB150077; RRID:AB_2630356
Alexa Fluor 555 conjugated goat anti-mouse ( <i>1:1000 dilution</i> )	Invitrogen	A-21422; RRID:AB_2535844
<b>Chemicals, peptides, and recombinant proteins</b>		
SR-101	Invitrogen	S359
Euthasol	Virbac	N/A
Triton X-100	Sigma	CAS: 9036-19-5
Sterilized EBSS	Worthington Biochemical	LK003188
Hybridization buffer	Molecular Instruments	N/A
Vectashield Antifade Mounting Medium DAPI	Vector Laboratories, Inc.	H-1200-10
UV-curing Optical Adhesive	Norland Products	NOA61
<b>Critical commercial assays</b>		
UBC-GFP Zebra finch genome sequencing (with Illumina NGS)	LC Sciences (Houston, TX)	N/A
Genomic DNA extraction and purification kit	New England Biolabs	NEB #T3010
<b>Deposited Data</b>		
Transgenic UBC-GFP Zebra finch genome	<i>This study</i>	SRA: PRJNA1061303 ( <a href="https://www.ncbi.nlm.nih.gov/sra/PRJNA1061303">https://www.ncbi.nlm.nih.gov/sra/PRJNA1061303</a> )
Cell migration data and analysis code	<i>This study</i>	Zenodo: ( <a href="https://github.com/naomish1230/Transgenic-songbird-neuron-migration">https://github.com/naomish1230/Transgenic-songbird-neuron-migration</a> )
<b>Experimental models: Organisms/strains</b>		
UBC-GFP transgenic zebra finches	Agate et al. <sup>12</sup> (bred in-house at Boston University)	N/A
<b>Oligonucleotides</b>		
GAD1	Molecular Instruments	(custom probe, RefSeq: XM_002198498)
VGLUT2	Molecular Instruments	(custom probe, RefSeq: NM_012000.1)
PDGFRA	Molecular Instruments	(custom probe, RefSeq: XM_030271078)
CSF1R	Molecular Instruments	(custom probe, RefSeq: NM_001193260.1)
UTS2B	Molecular Instruments	(custom probe, RefSeq: XM_0308048.3)
SLC15A2	Molecular Instruments	(custom probe, RefSeq: XM_030277156)
<b>Software and algorithms</b>		
FIJI	Schindelin et al. <sup>85</sup>	( <a href="https://github.com/fiji">https://github.com/fiji</a> ) RRID:SCR_002285
MATLAB	Mathworks	RRID:SCR_001622
Prairie View	Bruker	RRID:SCR_017142

(Continued on next page)

**Continued**

REAGENT or RESOURCE	SOURCE	IDENTIFIER
<b>Other</b>		
Glass micro-hematocrit capillary tube	Thomas Scientific	1202K16
Small bird stereotaxic frame	Kopf Instruments	Model 940 digital stereotaxic instrument with model 914 and 914T small bird adapter
Borosilicate capillary tubes	Drummond Scientific	N/A (100/VL – 3.5" length)
Small diameter round coverglass, #1 thickness, 3 mm diameter	Thomas Scientific	1217N66
Stainless steel cannula	Ziggy's Tubes and Wires	N/A (custom: 304 S/S Tubing; 125" OD x .115" ID x 0.019")
1.5 mm micro-prism with reflective hypotenuse	Tower Optical Corporation	Part Number: 4531-0023 ( <a href="https://www.toweroptical.com/micro-prisms/">https://www.toweroptical.com/micro-prisms/</a> )
Micro-knife	Fine Science Tools	Item No. 10316-14
Custom kinematic headplate	Kim et al. <sup>16</sup>	N/A
Sterile 1.5 mm biopsy punch	Royaltek	BP15
Vibratome	Leica	VT1000S
Confocal Microscope	Zeiss	LSM800
2P Microscope system	Bruker Corporation	N/A
Goniometric stage	ThorLabs	TTR001
7X-45X Binocular Stereo Zoom Microscope with Double Arm Boom Stand	AmScope	SKU: SM-4B
Infrared Camera	ELP	USB100W05MT-DL36

## RESOURCE AVAILABILITY

### Lead contact

Further information and requests for resources and reagents should be directed to and will be fulfilled by the lead contact, Dr. Benjamin B. Scott ([bbs@bu.edu](mailto:bbs@bu.edu)).

### Materials availability

Transgenic songbirds used in this study are available for use through materials transfer or collaborations upon request.

### Data and code availability

- Sequenced transgenic UBC-GFP zebra finch genome is available online (SRA: PRJNA1061303, <https://www.ncbi.nlm.nih.gov/sra/PRJNA1061303>).
- All data and analysis code necessary for main findings and figures is available online (Zenodo: <https://doi.org/10.5281/zenodo.1047669>, <https://github.com/naomish1230/Transgenic-songbird-neuron-migration>). Additional custom code will be available upon request.
- Any additional information required to reanalyze the data reported in this work paper is available from the [lead contact](#) upon request.

## EXPERIMENTAL MODEL AND STUDY PARTICIPANT DETAILS

Animal use procedures were approved by the Boston University Institutional Animal Care and Use Committee (IACUC; Protocol #201800577) and carried out in accordance with National Institutes of Health standards. Birds were housed under standard conditions (12h/12h light/dark cycle, access to dry food and water *ad libitum*). Both males and females (50–800 dph) were used throughout the study. Birds were bred at Boston University. Wildtype mates were bred to heterozygote transgenics generating offspring of known age. Offspring were screened for GFP expression using a 440–460 nm blue illumination and 500 nm longpass glasses (Night-sea). Hatchlings exhibit green fluorescence throughout their body while in juveniles and adults, GFP expression is most readily observable around the eye.

Transgenic UBC-GFP songbirds used in the study were previously created using lentiviral mediated trangensis.<sup>12</sup> To identify the transgene insertion site we used whole genome sequencing followed by alignment to the zebra finch genome (bTaeGut2.pat.W.v2, [https://www.ncbi.nlm.nih.gov/data-hub/genome/GCF\\_008822105.2/](https://www.ncbi.nlm.nih.gov/data-hub/genome/GCF_008822105.2/)) and plasmid FUGW (Addgene plasmid # 14883; <http://n2t.net/addgene:14883>; RRID: Addgene\_14883).

Genomic DNA was obtained from blood. The medial metatarsal vein in the leg of a male GFP+ zebra finch was nicked with a sterile 20 gauge needle. Blood was drawn with a glass Micro-Hematocrit capillary tube (Thomas Scientific). DNA was then extracted from 10 µL of blood using a genomic DNA extraction and purification kit (New England Biolabs). The sample was sent overnight on dry ice to a commercial next-generation sequencing company (LC Sciences, Houston, TX) for genome sequencing. Genome alignment to plasmid and reference genome was viewed in IGV, and allowed for insertion sites to be determined.

The UBC-GFP transgene was inserted on Chromosome 9. The insertion occurred in the range spanning positions NC\_045008.117066610 - NC\_045008.1:17066705, which is found within a gene called von Willebrand factor A domain containing 5B2 isolate (VWA5B2).

## METHOD DETAILS

### Surgical procedures

Stereotaxic surgery was performed on a Kopf Instruments 940 digital frame with a 914 small bird adapter. Anesthesia was maintained with 1–2% isoflurane in oxygen. Male birds were injected with a pulled borosilicate capillary tube (Drummond Scientific) into AreaX (head angle 20°, 5.8 mm anterior, 1.5 mm lateral, and 2.8 mm below the dura) with 90 nL of Dil (D3911, Fisher Scientific), dissolved to 5 mg/mL with dimethylformamide (Sigma). Female and male birds underwent a 3 mm craniotomy over HVC coordinates as the centerpoint (relative to the bifurcation of the midsagittal sinus: head angle 35°, 0.3 mm anterior, 2.1 mm lateral). For cranial window experiments, a 3 mm diameter round coverglass (3 mm circular, #1, Thomas Scientific), bonded to a stainless steel cannula (304 S/S Tubing .125" OD x .115" ID x 0.019"; Ziggy's Tubes and Wires, Inc., Sparta, TN) with UV-curing Optical Adhesive (#61, Norland), was placed over the exposed dura.

For prism experiments, a custom implant was created by attaching a 1.5 mm micro prism with a reflective hypotenuse (Tower Optical) to a cranial window (described above) with optical adhesive. A microknife (FST) attached to the stereotaxic arm was used to cut the dura. Then, the prism implant was slowly lowered into the brain (10 µm/s) with the stereotaxic arm, using vacuum suction, until the cranial window was flush with the inner skull. The cannula walls were secured to the surrounding skull with cyanoacrylate adhesive. A custom kinematic headplate<sup>16</sup> was secured to the skull with light-cured dental cement (Flow-It ALC, Pentron) and a curing LED 5W (NSKI, Amazon). The implant was covered with protective Kwik-Cast (VWR), which was removed before imaging. After recovery, finches were housed in a single cage in the colony room.

For allograft transplant experiments, transgenic zebra finches were anesthetized and underwent the craniotomy procedure over HVC (Table S2). Approximately 5–10 mg of tissue was dissected from HVC and the surrounding regions using a sterile biopsy punch (1.5 mm, Royaltek) and stored in sterilized EBSS (Worthington) on ice until implantation (<30 min). A wild type host bird received a craniotomy and approximately 1 mm<sup>3</sup> of tissue was removed via aspiration. Donor tissue was then gently fitted into the resulting cavity in the host brain. Gentle aspiration was applied peripherally to remove blood and saline. Surgery was concluded by replacing the host skull and sealing with silicone elastomer (Kwik-Sil, VWR) or by implanting a cranial window. Hosts were housed in a single cage within the colony for 3–9 weeks prior to sacrifice and histological characterization.

### Immunohistochemistry and characterization of GFP expression

Zebra finches were euthanized with Euthasol (Virbac) and perfused with 30 mL of 1X phosphate-buffered saline (PBS), followed by 50 mL of 4% paraformaldehyde (PFA). Brains were extracted and stored in PFA overnight. After fixation, brains were washed with PBS and sliced into 50 µm sections with a vibratome (Leica; VT1000S).

The primary antibodies used were: a rabbit polyclonal anti-GFP in a 1:400 dilution (Millipore Sigma, AB3080, lot: 3717722), a mouse monoclonal anti-NeuN in a 1:500 dilution that is a marker for mature neurons (Millipore Sigma, MAB377, clone A60, lot: 3612227),<sup>14</sup> a mouse monoclonal anti-DCX in a 1:400 dilution that is a marker for immature, migratory neurons (Santa Cruz Biotechnology, sc-271390 (E–6), lot: C3121),<sup>86–88</sup> a mouse monoclonal anti-Vimentin (40E-C-s) in a 1:10 dilution that is a marker for radial glia<sup>89</sup> (Developmental Studies Hybridoma Bank, AB528504), a mouse monoclonal anti-HuC/HuD that is a marker for cells in neuronal lineage<sup>13</sup> in 1:500 dilution (ThermoFisher Scientific A-21271). The secondary antibodies used were: Alexa Fluor 488 conjugated goat anti-rabbit (Abcam) and Alexa Fluor 555 conjugated goat anti-mouse (Invitrogen) in a 1:1000 dilution.

First, antigen retrieval was performed prior only to anti-HuC/HuD staining by incubating slices in a 50 mM solution of Tris buffer (Fisher Scientific) at a pH of 8.4 for 30 min. Then, for all immunohistochemistry, tissue sections were placed in a blocking solution composed of 2% nonfat dry milk (Great Value), 0.02% Triton X-100 (Sigma), and 1X PBS. Sections were incubated for 1 h at room temperature in primary antibody diluted in blocking solution, washed 3 times with PBS, then incubated with secondary antibody diluted in blocking solution for 1 h at room temperature or overnight at 4°C. Sections were mounted on microscope slides (Fisher Scientific) using Vectashield Antifade Mounting Medium with DAPI (Vector Laboratories, Inc.). Histological fluorescent images were acquired using a confocal microscope (Zeiss LSM800, Germany).

Image processing was performed with FIJI/ImageJ.<sup>85</sup> To quantify levels of co-expression between GFP and other proteins in song nucleus HVC, we focused on cells within HVC. HVC could be identified by dimmer background GFP expression relative to surrounding areas (Figure S1). In young juveniles and females with no distinct difference in GFP expression in HVC, all region-of-interests (ROIs) were randomly selected in the area below the ventricular zone that corresponded to stereotaxic HVC coordinates. Individual ROIs were manually drawn around cell bodies in single Z-planes in one isolated channel. The tracer was blinded to the other

channel's expression within that ROI. ROIs were then overlaid on the second channel for analysis, mean intensity in the GFP channel was measured, and ROIs were manually scored as colocalizing or not colocalizing with another antibody. Analysis was performed in Google Sheets or MATLAB.

#### **Fluorescent *in situ* hybridization chain reaction (HCR-FISH)**

Fluorescent *in situ* hybridization chain reaction (HCR-FISH) was performed using custom probes designed by Molecular Instruments for detection of zebra finch *GAD1*, *VGLUT2*, *PDGFRA*, *CSF1R*, *SLC15A2*, and *UTS2B* mRNA (See [Key Resources table](#)), which are cell type markers selected from previous scRNAseq studies.<sup>6</sup> Birds were perfused with formalin and brains were post-fixed in formalin overnight at 4°C. Brains were sectioned on a LEICA VT 1000S into 150 µm slices and collected in 1X RNase-free PBS. Slices were incubated in 90% DMSO/RNase-free PBS for 2 h at room temperature and then in 1% NaBH4/RNase-free PBS for 15 min at room temperature. The slices were then incubated in 8% SDS/RNase-free PBS for 1.5 h at room temperature. Then, the slices were washed three times for 1 h in 2X sodium chloride sodium citrate 0.1% Tween 20 (2X SSCT) at room temperature and then washed in probe hybridization buffer (Molecular Instruments) for 30 min at 37°C. The slices were hybridized overnight at 37°C in a solution containing 4 nM of each probe in hybridization buffer (Molecular Instruments). On the second day, the slices were washed four times in wash buffer (Molecular Instruments) at 37°C and three times in 5X SSCT for 5 min at room temperature. Then they were incubated in an amplification buffer for 30 min at room temperature. Lastly, they were incubated overnight in a solution containing 2µL of fluorescent-carrying hairpins per 200µL of solution (Molecular Instruments) at room temperature. The next day, slices were washed three times in 5X SSCT and one time in 5X SSC at room temperature. They were then fixed for 20 min in PFA 4% at room temperature. Subsequently, immunohistochemistry staining was performed using the following antibodies: rabbit polyclonal antibody against GFP in 1:400 dilution (Millipore Sigma, AB3080, lot: 3717722) and Alexa Fluor 488 conjugated goat anti-rabbit in 1:500 dilution (Abcam). All images were acquired using a confocal microscope (Zeiss LSM800, Germany) and loaded into FIJI/ImageJ for quantitative HCR-FISH staining analysis in the manner described above.

#### **Two-photon (2P) microscopy**

Imaging was performed on a commercial 2P microscope system (Bruker Corporation, Prairie View Software). GFP, sulforhodamine-101, and Dil were excited by near-infrared light (920 nm) produced by a titanium:sapphire laser (Spectra-Physics, Insight X3; or Coherent, Chameleon Ultra II). Post objective power was less than 100 mW for all imaging experiments. Images were acquired using a Nikon 16X, 0.80 NA water-immersion objective lens (ThorLabs, N16XLWD-PF), or an Olympus 20X, 0.50 NA water-immersion objective lens (Olympus, UMPLFLN20XW), and photomultiplier tubes (Hamamatsu, H10770PB-40).

Imaging was performed in head-fixed and body restrained unanesthetized animals. Headplates were attached magnetically to a custom kinematic fixation system<sup>16</sup> on top of a goniometric stage (ThorLabs) while the animal was restrained in a custom foam restraint. A custom 3D-printed conical well was fastened to the headplate with silicon elastomer to hold water for longer time-lapse sessions. The animal was observed with an infrared camera (USB100W05MT-DL36, ELP, iSpy Software). Time intervals varied per animal ([Table S3](#)). In some sessions the Z-stacks were sampled in succession (~10 min interval between frames) for up to 3 h. In longer sessions, time-lapses were acquired intermittently at intervals ranging from 20 min to up to an hour between Z-stacks for 5–12 h. Between intermittent imaging timepoints, the animal was freed from restraint and returned to its cage with food and water. In some sessions, the animal was injected IM with 50 µL of 20 mM SR-101 (Invitrogen) before the last time point to label the blood vessels in the volume.

#### **QUANTIFICATION AND STATISTICAL ANALYSIS**

##### **Image processing and data analysis**

All data was stored and accessed on Boston University's Shared Computing Cluster. Session images were loaded into FIJI as 4D hyperstacks. A denoising algorithm was applied to the hyperstacks using FIJI functions in the following order: Background Subtraction, a Gaussian high pass filter, Median Filter, Despeckle. Hyperstacks were registered with the Correct 3D Drift plug-in in FIJI. The session data was first split up by brain region, and then split up into four quadrants for easier distribution to trackers and management for tracking. The centerpoint of migratory cells was identified by expert trackers across time using a custom macro script in FIJI that enabled the use of Orthogonal Views and sequential ROI selection with the Multi-Point Tool.

All track analyses were performed using custom scripts in MATLAB. Tracking data was pre-processed to remove duplicate tracks and erroneous points. Cells that traveled less than 5 µm and cells with tortuosities above 7 were removed.

To evaluate the degree of "association" of migrating cells with vasculature, tracks from imaging sessions with SR-101-labeled blood vessels were evaluated in FIJI. After the GFP channel was isolated and migratory GFP+ cells were tracked by expert trackers, GFP and SR-101 channels were recombined. Expert scorers overlaid tracked ROIs (the centerpoint of each cell across time) and recorded the position at that time point as an "association" if the ROI came within 1 µm of SR-101-positive vasculature. Length of associations were determined by computing the distance traveled by cells that had ROIs closely associated with SR-101 labeled vasculature for multiple timepoints consecutively.

Custom scripts in MATLAB were used to fit a power law model to either the MSD of individual cells or the average MSD from entire cell populations to extract the  $\alpha$  parameter. This was done using the MATLAB fit function, with 'power1' specified as the model.  $\alpha$  fit to individual cells was only considered if it was less than 4 and the  $R^2$  value of the fit was above 0.95.

### Statistical tests

All statistical tests were conducted using MATLAB. Rayleigh's test for circular uniformity was used to test for directional bias in Figure 4F. Two-sample t-tests were used to test for a difference between two groups, such as in the  $\alpha$  parameter between superficial and deep migrating cells in Figure 6G, for example. To test for linear relationships between heading or speed and distance between cell pairs in Figures 5B–5D, linear regression models were fitted. We similarly employed Spearman's rank correlation coefficient to assess the strength and direction of association between two variables, such as heading or speed and distance between cell pairs. We shuffled distributions, such as in Figures 5A–5C, to compare population correlations to chance levels. To compare data distributions to shuffled distributions, such as in Figures 5A–5C, we used a two-sample Kolmogorov-Smirnov test. All statistical details of experiments can be found in figure legends, as well as in the Results sections. These details include: the statistical test used, the exact value of n, what n represents (number of birds, number of cells, etc.), as well as the mean values and the standard deviations.

### Migration simulation

The migration simulation was written in MATLAB. HVC was represented as a 1 mm diameter sphere intersected by a tilted plane (representing the VZ) and has a comparable volume and shape as HVC found in zebra finches.<sup>35,90</sup>

A simulation run began with the birth of a cell in the VZ at a randomly selected point on the VZ-HVC interface. Each cell (represented as a vector with position P and heading H) was born heading in a random 3D direction which serves as the cell's initial H. At each timepoint (whose real world equivalent duration is 10 min) a cell takes a step of distance d in the direction H<sub>t</sub>. d is drawn from a log-normal distribution ( $\mu = 0.83 \mu\text{m}$ ,  $\sigma = 0.79 \mu\text{m}$ ) and  $\Delta a$  is drawn from a logistic distribution ( $\mu = -1.38^\circ$ ,  $\sigma = 9.79^\circ$ ,  $p = 0.9$ ) with a uniform offset (ranging from  $-180^\circ$  to  $180^\circ$ ,  $p = 0.1$ ; Figures 7A, S7A and S7B). These distributions were derived from step sizes and angle changes measured from *in vivo* cell migration data recorded at  $\sim 10$  min intervals (see *Validation of migration simulation against experimental data below*).

Cells are prevented from crossing the VZ at any point during their migration: if P<sub>t</sub> is on the other side of the VZ, d and  $\Delta a$  for that step are redrawn.

### Validation of migration simulation against experimental data

In order to validate the design of the simulation, three main metrics were recorded to compare simulation output with cell tracking data: speed, tortuosity, and the  $\alpha$  parameter derived from the curve fit to the MSD across time intervals. Each of these parameters were measured per cell for the entirety of their migration. These metrics were gathered from simulations that spanned a nearly identical time interval and window as that of cell tracking experiments (10 min time interval, 3 h tracking window) in order to be able to draw direct comparisons between the outcomes of the simulation and tracking data. A two sample t test revealed that there was no significant difference in the tortuosity measured between the simulation and the tracking experiments, suggesting that the simulation was successful in recapitulating tortuosity dynamics that were observed *in vivo* (n = 143 cells,  $p_{\text{tort}} = 0.0967$ ) (Figure S7F). Distributions of well-fit ( $R^2 > 0.95$ ) individual  $\alpha$ 's measured for each trajectory were well-described by log-logistic distributions for both the simulated and tracked cell populations (n = 110 cells,  $\mu_{\text{sim}} = 0.50$ ,  $\sigma_{\text{sim}} = 0.055$ ,  $\chi^2_{\text{sim}} = 7.35$ ,  $p_{\text{sim}} = 0.12$ ,  $\mu_{\text{track}} = 0.51$ ,  $\sigma_{\text{track}} = 0.15$ ,  $\chi^2_{\text{track}} = 9.41$ ,  $p_{\text{track}} = 0.052$  (Figures S7G–S7H). Although both had a similar distribution peak, there was a noted difference in  $\sigma$ , indicating that although the average  $\alpha$  from the simulation matches the observed  $\alpha$  from *in vivo*, the population variability of  $\alpha$  is not entirely recapitulated (Figure S7E). It should be noted that the average population  $\alpha$  measured across 10 simulation runs is 1.535 (n = 10,000 cells,  $\sigma = 0.0116$ ), which defines the movement of simulated cells as superdiffusive. This superdiffusive mean population  $\alpha$  is nearly identical to the mean population  $\alpha$  recorded across 8 birds during tracking experiments ( $\mu_{\text{track}} = 1.5385$ ) (Table S4). For speed, a two sample t test indicated a significant difference ( $p_{\text{speed}} \leq 0$ ) between the simulation and tracking experiments although there is overlap between the two groups' standard deviations. However, the distributions of step size from the tracking experiments and the simulation are highly similar (paired sample t test,  $p = 0.5341$ ) (Figure S7C), suggesting that the difference in measured speed originates either from the simulation's assumption of independent stochastic step and heading selection, or the frequent migratory pauses cells take *in vivo* that are not accounted for in the simulation (see Figure S8).

Simulated cells in these validation experiments began their migrations at random points throughout HVC, not in the VZ, as tracked cells were distributed throughout the volume at the time of their recording. Speed was calculated as the sum of all distances traveled divided by the duration of migration. Tortuosity was measured as the ratio between the length of the path traveled by a cell to the shortest distance between its start and endpoints. Log-logistic curves were fitted to the distributions of individual cells'  $\alpha$  using MATLAB's custom distribution fitter. In addition to calculating the individual  $\alpha$  for each cell's migration, the population  $\alpha$  was assembled from every cell simulated within a single run by taking the average of the MSD at each  $\tau$  across all cells to form a single MSD curve that was representative of the simulated population.

**Simulation extrapolation analysis**

Once this model had been validated against the tracking data over a 3 h time window, the simulation was run for 40 days to observe if superdiffusive dynamics could be successfully extrapolated to biologically relevant timescales. For these experiments, cells were born in the VZ to observe their behavior and spread for the entirety of their lifespan. To assess whether HVC was sufficiently populated, we took the average of each cells' minimum distance from the VZ across 5 simulation runs with each run containing 1000 cells. This distance was calculated and compared to the center of mass of the virtual HVC: for Figure 7D, the minimum distance was recorded per cell at the end of each day of migration. A similar process was used to calculate the average maximum distance of each cell from the VZ over 40 days to see how far cells could migrate away from their birthplace. Additionally, the Shannon entropy (see [Calculating entropy](#) below) of the final positions and headings of 1000 cells simulated over 21 days were compared to entropy of the positions and headings of tracked cells at the end of 3 h of tracking. Simulated endpoints were recorded from cells that fell within the FOV used during cell tracking at the end of each day of migration; likewise, simulated cell headings were calculated as the vector between the cell's final position and its position 3 h prior to its migration ending when both its final and 3 h prior position fell within the aforementioned FOV. This FOV, which was a 3D volume ( $350 \times 400 \times 300 \mu\text{m}$ ), was based on cell tracking experiments and permits for direct comparisons to be drawn between the simulation output and the tracking data.

**Estimation of angle and step size distributions****Angle**

The  $\Delta a$  distribution was obtained by fitting a logistic distribution to the histogram of XY plane angle change ( $\Delta a_{XY}$ ) measured from tracking individual cells *in vivo* during cranial window 2P imaging conducted in transgenic finches. 143 cells were tracked over approximately 3 h in two juvenile male birds with cells recorded in HVC (pink61 and gray3L). Artifacts resulting from the manual cell tracking process were reduced by excluding recorded  $\Delta a_{XY}$  when a cell migrated less than  $5 \mu\text{m}$  before or after the  $\Delta a_{XY}$ . Based on prism tracking experiments that indicate that cells migrate similarly in both XY and XZ (see Figures S3 and S4), the  $\Delta a_{XZ}$  distribution was inferred to be identical to  $\Delta a_{XY}$ . A logistic distribution was determined to be the distribution of best fit to the  $\Delta a$  data based on a maximum log likelihood estimation. In order to account for rarer, but observed cases in which cells made broad ( $>90^\circ$ ) turns between steps, a secondary uniform distribution ( $\mu = 0^\circ$ ,  $\sigma = 103.92^\circ$ ) ranging from  $-180^\circ$  to  $180^\circ$  was included in creating  $\Delta a$ . At the beginning of each step,  $\Delta a_{XY}$  and  $\Delta a_{XZ}$  are independently and randomly generated for a cell. When either of these  $\Delta a$  are generated, it will randomly select this angle change from the primary logistic distribution with a 90% probability, and from the secondary uniform distribution with a 10% probability.

**Step size**

The distance  $d$  that a cell will traverse over a single simulated step is randomly selected from a continuous lognormal distribution fit to the distribution of step distances from the aforementioned 2P cell tracking data.

**Calculating entropy**

The Shannon's entropy of the final recorded positions of the tracked cells and of the final positions of the simulated cells was calculated as follows:

$$\text{Entropy} = - \sum p(C_b) * \log(p(C_b))$$

where  $p(C_b)$  is the normalized probability that a cell's position is within any spatial bin when bin size is gradually increased. For each iteration of entropy calculated, the number of bins was increased by one, beginning with 3 bins and iterating until 200 bins. The number of cells within each bin is counted and the probability that a cell is in any of the bins,  $p(C_b)$ , is calculated and normalized to the total number of cells present in all bins. Inserting this probability into Shannon equation allows us to calculate the average entropy of the cells across the entire FOV. A similar approach was utilized when calculating the heading entropy of both tracked and simulated cells with heading being considered instead of the cell's final recorded position.

To create a maximum entropy model simulation, we performed the same procedure as for entropy calculations but assumed a multinomial uniform distribution by setting a constant probability of cells being in a bin.